Universidad de Cantabria

Facultad
de
Ciencias

La influencia de incertidumbres sistemáticas en la cosmografía con retardos temporales en cúmulos de galaxias

The impact of systematic uncertainties in cluster time-delay cosmography

Trabajo de Fin de Grado
para acceder al

GRADO EN FÍSICA

Autora: Elena Ruiz Ruiz

Directora: Ana Acebron Muñoz

Julio de 2025

Gracias a mis padres y a mi hermano, que han aguantado cuatro años de quejas interminables y me han apoyado en todo momento.

Gracias a mi familia y a mis amigos: a los que ya conocía cuando empecé este camino, y a los que he conocido en el proceso, tanto en Santander como en Belfast, por creer en mí cuando ni yo misma lo hacía.

A todos mis compañeros, por acompañarme en ese sufrimiento que nadie más que nosotros entiende.

A todos mis profesores,
en especial a Ana,
gracias por confiar en mí y ayudarme a sacar este trabajo adelante, por aconsejarme y por enseñarme esos pequeños detalles que pueden marcar la diferencia.

Resumen

La constante de Hubble, H_0, determina el ritmo de expansión del Universo, y ha sido (y es) una de las medidas más buscadas en cosmología. Se han realizado numerosas exploraciones para medir este parámetro fundamental, que determina el tamaño, la edad y la densidad crítica, $\Sigma_{\rm crit}$ del Universo. Comprender el impacto de las posibles fuentes de incertidumbre en cada técnica es crucial. En concreto, este trabajo está centrado en las lentes gravitacionales fuertes.

A lo largo de las últimas décadas, la cosmografía con retardo temporal en lentes gravitacionales fuertes se ha convertido en una de las técnicas más prometedoras para medir el valor de H_0, aunque todavía queda mucho por descubrir. Las lentes gravitacionales fuertes se refieren al fenómeno en el que la luz de fuentes lejanas se dobla a causa de objetos masivos, como galaxias o cúmulos de galaxias. Este efecto puede producir arcos gigantes e imágenes múltiples de las fuentes del fondo. La propagación de los rayos de luz de una fuente de fondo hasta un observador depende tanto de la longitud geométrica del camino como del potencial gravitatorio (o masa total) que experimenta el rayo de luz. En consecuencia, los rayos de cada imagen múltiple de una misma fuente llegan al observador en distintos momentos. Esto se conoce como retardo temporal. Estos retardos temporales se pueden medir por monitorización fotométrica, cuando la fuente de fondo es un objeto intrínsecamente variable, como los cuásares, y son principalmente sensibles al valor de H_0.

Para medir el valor de H_0, se necesita modelar con gran precisión la distribución de masa total de la lente. En este trabajo, se ha explorado el impacto de distintas opciones de modelo y suposiciones en el valor medido de H_0 en un único cúmulo lente, SDSS J1029+2623. Para hacerlo, se ha utilizado un nuevo software de modelización de lentes gravitacionales fuertes, `gravity.jl`, que es considerablemente más rápido que otras herramientas en el campo.

Analizamos 15 modelos de lente para estudiar el efecto de varias fuentes de errores sistemáticos en SDSS J1029+2623, caracterizado por siete sistemas fuertemente lensados, uno de los cuales es un cuásar. El sistema del cuásar muestra tres imágenes múltiples, de las que se ha obtenido un retardo temporal, de unos 744 días. Hemos explorado y cuantificado el efecto de variaciones en el catálogo de galaxias miembro e imágenes múltiples, perfiles de densidad de masa y modelos cosmológicos. El modelo `Fiducial` produce un valor de la constante de Hubble de $H_0 = 93.7 \pm 18.8$ km s^{-1}Mpc^{-1}; y el modelo `Combined`, $H_0 = 93.7 \pm 20.1$ km s^{-1}Mpc^{-1}. También hemos inferido valores de los parámetros de densidad de materia media y de la ecuación de estado de la energía oscura, Ω_m y w. Los valores del primero van desde $\Omega_m = 0.3$ hasta $\Omega_m = 0.5$, con elevados errores relativos. El valor de w se infiere en $w = -1.1 \pm 0.3$. Se observa un potencial efecto de una hoja de masa, que puede indicar que hay fuentes de incertidumbre aún por explorar en el modelo, y puede ser la razón por la que los valores de H_0 no coinciden ni con los del Universo temprano ni con los del tardío.

Se espera que los avances en instrumentación y un conjunto de datos más extenso mejoren considerablemente los resultados obtenidos de la cosmografía con retardos temporales en cúmulos de galaxias. Las próximas inspecciones de campo amplio pronto descubrirán un muestrario estadístico de sistemas únicos, mientras que las imágenes del infrarrojo cercano nos permitirán identificar más imágenes múltiples que restrinjan los modelos de lente.

Abstract

The value of the Hubble constant, H_0, which determines the rate of expansion of the Universe, has been one of the most long-sought measurements. Several cosmological probes have been used to measure the value of this fundamental parameter, which sets the size, age or critical density, $\Sigma_{\rm crit}$ of the Universe. Understanding the impact of the possible systematic uncertainty sources within each technique is crucial. In this work, we have focused on strong lensing.

In the last decades, strong lensing time-delay cosmography has become one of the most promising methods to measure the value of H_0, but remains considerably unexplored. Strong-lensing refers to the phenomenon of the bending of light from distant sources caused by intervening massive objects, like galaxies and galaxy clusters. This effect can produce giant arcs and multiple images of background sources. The propagation of light rays from a background source to the observer depends both on the geometrical length of the path and on the gravitational potential (or total mass) experienced by the light ray. As a result, it takes different times, known as time delays, for the light rays to reach the observer from each multiple image of the same source. These time delays can be measured through photometric monitoring, when the background source is an intrinsically time-varying object, such as quasars, and are primarily sensitive to the value of H_0.

To measure the value of H_0, one needs to model with high accuracy and precision the total mass distribution of the lens. In this work, we have explored the impact of different modelling choices and assumptions on the measured value of H_0 with a unique lensing cluster, SDSS J1029+2623. To do so, we have used a new strong-lensing modelling software, `gravity.jl`, which is considerably faster than other tools in the field.

We analyse 15 lens models to study the effect of several sources of systematics in SDSS J1029+2623, characterised by seven strongly-lensed systems, one of which is a quasar. The quasar system shows three multiple images for which we have also exploited one measured time delay, of about 744 days time delay. We have explored and quantified the effect of variations in the cluster member catalogue, the multiple images catalogue, mass-density profiles and cosmological models. The `Fiducial` model yields a value of the Hubble constant of $H_0 = 93.7 \pm 18.8$ km s^{-1}Mpc^{-1}; and the `Combined` model, $H_0 = 93.7 \pm 20.1$ km s^{-1}Mpc^{-1}. We have also inferred values for the mean matter density and the dark energy equation of state parameters Ω_m and w. Values for the first one range between $\Omega_m = 0.3$ and $\Omega_m = 0.5$, with large relative errors. The value of w is inferred as $w = -1.1 \pm 0.3$. A potential mass sheet effect is observed, which may indicate unexplored uncertainties in the model, that can also be the reason why the inferred values of H_0 are not in agreement with the early or late Universe values.

Advances in instrumentation and a larger dataset are expected to highly improve the results obtained from strong lensing time-delay cosmography with galaxy clusters. Upcoming wide-field surveys will soon unveil a statistical sample of such unique systems while high-resolution near-infrared imaging will allow us to identify more multiple images that further constrain the lens models.

Table of contents

1 Introduction **1**

1.1 Motivation and structure . . . 1

1.2 The Universe: galaxies and cosmology . . . 1

1.2.1 Galaxies . . . 2

1.2.2 Galaxy clusters . . . 5

1.3 Gravitational lensing . . . 7

1.3.1 Time delays . . . 9

1.3.2 Simple mass-density distributions . . . 10

1.3.3 Cosmography with lens galaxy clusters . . . 11

1.3.4 State-of-the-art . . . 11

1.4 The Hubble constant . . . 12

2 Parametric Strong Lensing Modelling of Galaxy Clusters **14**

2.1 Observables . . . 14

2.1.1 Positions of multiple images . . . 14

2.1.2 Time delays . . . 16

2.1.3 Flux ratios . . . 16

2.2 Mass density distributions . . . 16

2.2.1 Dark matter halos . . . 16

2.2.2 Cluster member galaxies . . . 17

2.2.3 External shear . . . 17

2.3 Scaling relations . . . 17

2.4 `Gravity.jl` . . . 18

3 SDSS J1029+2623 **21**

3.1 Discovery . . . 21

3.2 Main features and description 21
3.3 Spectro-photometric data 23
3.4 State-of-the-strong-lensing analyses 24

4 Results **28**
4.1 Strong lensing models 28
4.1.1 Cluster members catalogue 28
4.1.2 Multiple images catalogue 29
4.1.3 Mass parametrisation 30
4.1.4 Alternative cosmological models 32
4.2 The influence of systematics in SDSS J1029+2623 34
4.2.1 Statistical estimators 34
4.2.2 H_0 inference 36
4.2.3 Mass sheet 37
4.2.4 General cosmologies 38
4.3 Testing `gravity.jl` 39
4.3.1 Rescaling of the positional uncertainties 39
4.3.2 Variational rounds 39
4.4 Discussion 41

5 Conclusions and perspectives **42**

1 Introduction

1.1 Motivation and structure

Strong lensing in galaxy clusters is a promising technique to probe both dark matter and dark energy and thus measure the geometry and the expansion rate of the Universe. This technique is completely independent to other well-established cosmological probes, but as for any of them, the study of systematic uncertainties is crucial and, in particular, how they can potentially affect the model-predicted time delays, and hence the Hubble constant. Actually quantifying how each of the systematics affects the results is fundamental, especially in the era of precision cosmology.

This project presents an ensemble of different sources of systematic uncertainties and analyses their impact on the strong lensing galaxy cluster SDSS J1029+2623. An initial introduction explaining the foundation of strong lensing and the composition of the Universe is presented in Chapter 1. The parametric strong lensing modelling technique is described in Chapter 2, where we look deeper into how the analyses should be done: the observables we find in our lens system, parametrisation techniques and the software used in this work, `gravity.jl` (Lombardi 2024). Later we will present the strong lensing cluster itself, providing some historical context and detailing its main features, including the data and previous strong lensing analyses, all in Chapter 3. Finally, all the models studied and their results will be presented and discussed in Chapter 4, and the conclusions will be summarised in Chapter 5.

1.2 The Universe: galaxies and cosmology

Less than 5% of the vast Universe is made up of baryonic matter which is, in other words, regular matter. This includes stars, planets, gas, and dust: anything made up of atoms and molecules. Around 25% of the matter is in the form of dark matter, which only interacts through gravity. The remaining 70% of the Universe energy density is qualified as dark energy. Dark energy is considered responsible for the accelerated expansion of the Universe. However, both the actual extent of the effects of dark matter and dark energy, as well as their nature and properties, are highly mysterious. This motivates the study of techniques that allow one to probe the dark components of the Universe.

In this work, we have focused on the strong lensing modelling of galaxy clusters to measure the values of key cosmological parameters. In this Chapter, we first introduce the most basic components of the Universe: galaxies and galaxy clusters, in Section 1.2. We then present, in Section 1.3, the modelling technique we use: strong gravitational lensing. Finally, in Section 1.4 we introduce the Hubble constant, that leads the motivation of this investigation.

1.2.1 Galaxies

Galaxies can be thought of as the basic building blocks of the Universe. They are an ensemble of stars, planets, dust, gas, dark matter... All of these objects are bound together through gravity. It is now widely established that all galaxies harbour a super-massive black hole in their centres that can accrete matter. If enough matter is dragged into the black hole, it can eventually emit large amounts of radiation, giving rise to one of the brightest and strongest phenomena in the Universe, quasars.

There are several ways to classify galaxies: according to their morphology, their luminosity, or colours. The most widely spread and historical classification is according to their shape with the so-called Hubble diagram, shown in Figure 1.1. Morphological classification is very intuitive, but can also be very confusing. The orientation of a galaxy can lead to errors when determining its ellipticity; however, there are several factors that determine the morphology of a galaxy. Important information can also be obtained from the brightness of a galaxy, because the more massive a galaxy is, the brighter. Galaxies can be classified into three different main types according to their morphology: spirals, ellipticals, and irregulars. Moreover, there are other types of galaxies, such as S0, which are an intermediate phase between spirals and ellipticals; or active galaxies, characterised by the strong source in the centre (like quasars).

Spiral galaxies consist of a central bulge and an arm structure, external disk. They might also have a bar crossing the central bulge, separating spirals into barred spirals and normal spirals. Spiral galaxies contain younger stars, which typically have lower metallicity and are bluer, indicating a high star formation rate.

On the other hand, elliptical galaxies span a range of absolute magnitudes that, in the B-band, goes from -8 (faintest) to -25 (brightest). They have no clear structure and can be classified according to the ratio between the major axis, a and the minor axis b, which we call ellipticity. Most of the galaxies have large amounts of gas at different temperatures and prominent dust disks. Their rotation velocity, $v_{\rm rot}$, is much lower than the dispersion velocity, σ_0, hence the ellipticity of a galaxy is mostly not due to rotational effects, as was initially believed. Instead, it is now believed that the observed ellipticity is due to the anisotropic distribution of stars along the potential of the galaxy. They have an older stellar population and, therefore, the stars look redder. Redness is accentuated in the centre of the galaxy, where the metallicity is higher. They present a star formation rate so low that it does not affect the colour of the galaxy.

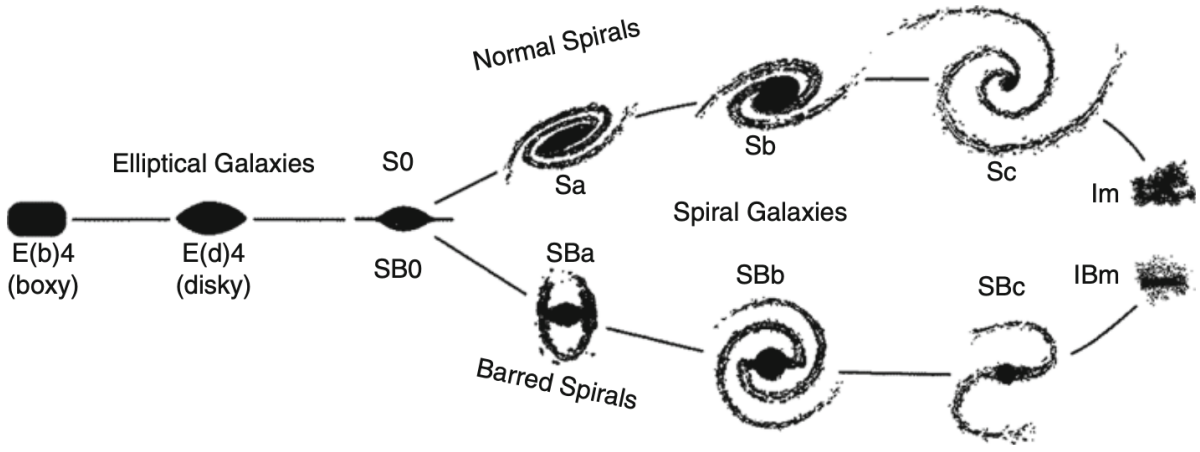

Figure 1.1: Hubble's 'tunning fork' for galaxy classification. Adapted from: J. Kormendy & R. Bender 1996, A Proposed Revision of the Hubble Sequence for Elliptical Galaxies, ApJ 464, L119, Fig. 1. c AAS.

This morphological classification can be summarised into *late-type* galaxies, which include irregulars and spirals; and *early-type* galaxies, which include S0 and ellipticals. *Late-type* galaxies can evolve into *early-type* galaxies through major mergers, but the Hubble diagram is not thought of as an evolutionary track.

Scaling relations

Galaxies are characterised by a number of properties that can be observed or measured. These properties can be related to each other, or to other intrinsic properties such as the mass using scaling relations. For elliptical galaxies, which are overwhelmingly found in the cores of galaxy clusters, there are two particularly useful scaling relations: the Faber -Jackson and fundamental plane.

The Faber-Jackson relation

The Faber-Jackson relation is specific for elliptical galaxies, and relates the luminosity of a galaxy, L, with its central velocity dispersion, σ_0 (which can be linked to its total mass) following the expression below:

$$L \propto \sigma_0^4, \tag{1.1}$$

which can be derived from the Virial theorem:

$$2K + U = 0, \tag{1.2}$$

where K is the kinetic energy and U is the potential energy of the galaxy.

If a dynamical system satisfies the Virial theorem (Eq. (1.2)), it is in stationary equilibrium. From the regular equations for kinetic and potential energies, we obtain

$$M\sigma_0^2 - \alpha\frac{GM^2}{R} = 0 \qquad \rightarrow \qquad M \sim \alpha\frac{\sigma_0^2 R}{G}. \tag{1.3}$$

M and R are the mass and radius of the galaxy, G is the gravitational constant, and α is a dimensionless scaling parameter.

If we project the velocity dispersion onto the plane, $\sigma_0^2 \approx 3\sigma_{r,0}^2$, and we introduce the mass-to-light ratio, M/L, we get

$$L \propto \frac{R\sigma_{r,0}^2}{G(M/L)}. \tag{1.4}$$

Since we empirically know that

$$L \propto \langle I \rangle_e R^2, \tag{1.5}$$

where $\langle I \rangle_\mathrm{e}$ is the mean surface brightness, we can plug this into our Eq. (1.4), substituting R. If we square the equation, we get to the Faber-Jackson relation in Eq. (1.1).

Fundamental plane

The fundamental plane implies a relation between the effective radius, R_e and the average surface brightness of the galaxy, $\langle I \rangle_\mathrm{e}$. Starting from the Kormendy relation, we can equate these two terms as follows:

$$R_\mathrm{e} \propto \langle I \rangle_\mathrm{e}^{-0.83}. \tag{1.6}$$

Hence, the total luminosity of a galaxy is

$$L = 2\pi R_\mathrm{e}^2 \langle I \rangle_\mathrm{e}. \tag{1.7}$$

Using again Eq. (1.5) we can obtain the relation

$$L \propto \langle I \rangle_\mathrm{e}^{-0.66}. \tag{1.8}$$

This proves there is a relationship between L and $\langle I \rangle_\mathrm{e}$. If we also account for Eq. (1.1), the relationship also applies for σ_0. However, the exponents that we would theoretically get from this derivation differ from the observed ones. Indeed, the empirical fundamental plane relation is

$$R_\mathrm{e} \propto \sigma_0^{1.4} \langle I \rangle_\mathrm{e}^{-0.85}. \tag{1.9}$$

The fundamental plane can also be derived from the Virial theorem. Following the same steps as for the Faber-Jackson relation we reach Eq. (1.4) that, if substituted using Eq. (1.5) leads to

$$R \propto \frac{\sigma_{r,0}^2}{\langle I \rangle_\mathrm{e}} \frac{L}{M} \propto \frac{\sigma_0^{1.4}}{\langle I \rangle_\mathrm{e}^{0.85}}. \tag{1.10}$$

When compared to Eq. (1.9) we get

$$\frac{M}{L} \propto \frac{M^{0.3}}{R_\mathrm{e}^{0.3}} \frac{R_\mathrm{e}^{0.3}}{L^{0.15}}. \tag{1.11}$$

The M/L can be expressed as

$$\frac{M}{L} = \frac{L^{2\alpha} L^{\beta}}{L}. \tag{1.12}$$

α and β are dimensionless exponents that determine the tilt of the fundamental plane. To determine their value, we can say

$$2\alpha + \beta - 1 = 0.2. \tag{1.13}$$

The tilt of the fundamental plane has been empirically measured to be

$$\frac{M}{L} \propto M^{0.2} \quad ; \quad \frac{M}{L} \propto L^{0.25}. \tag{1.14}$$

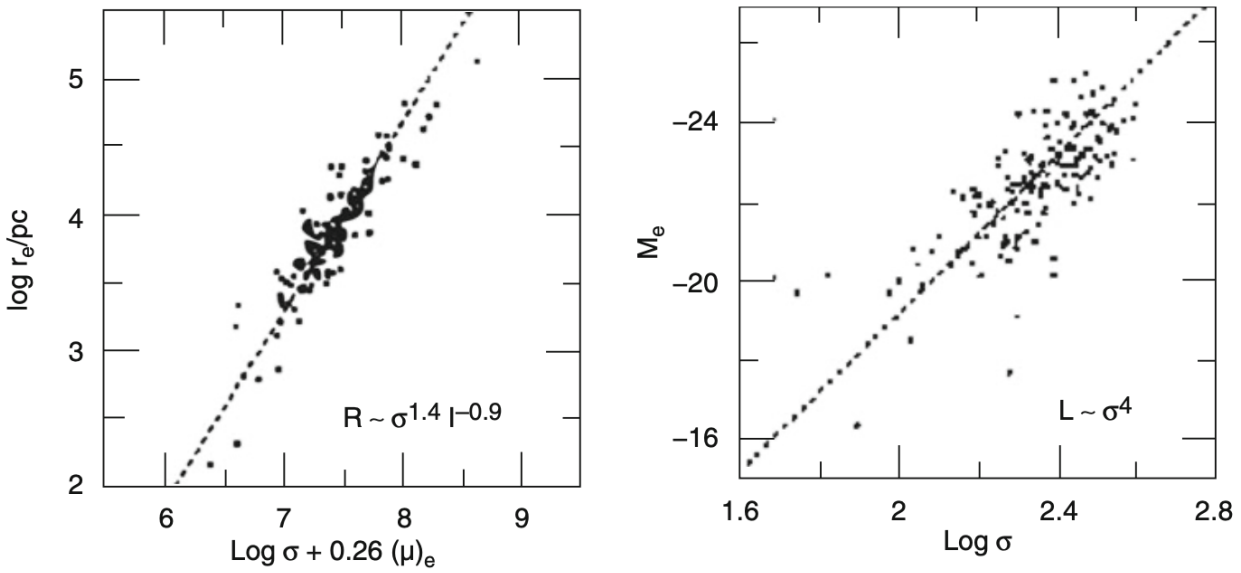

Figure 1.2: Projection of the fundamental plane for different parameter planes. To the left we find the lateral view of the fundamental plane. To the right we have the Faber-Jackson relation. Adapted from: J. Kormendy & S. Djorgovski 1989, Surface photometry and the structure of elliptical galaxies, ARA&A 27, 235, Fig. 2, p. 255.

The Faber-Jackson relation shows a higher dispersion than those from the fundamental plane, as can be seen in Figure 1.2.

1.2.2 Galaxy clusters

When several galaxies are gravitationally bound, we have a group of galaxies or a galaxy cluster. Galaxy clusters make up the overdense regions of the Universe. They can contain up to thousands of cluster members. Out of the total mass of a cluster, only around 4% is related to stars. Between 10 and 15% is also baryonic mass, but in the form of a X-ray emitting hot gas that constitutes the intracluster medium. The remaining $\sim$ 85% of their total mass is in the form of dark matter and, as mentioned before, highly contributes to the gravitational behaviour of the cluster.

Most clusters have a higher density towards the centre, and are mainly formed by elliptical galaxies. Cluster members can be found using the red sequence. In a colour-magnitude diagram, the galaxies with similar features populate a specific narrow region of this parameter space: they were formed approximately at the same time and have similar stellar populations (and thus colours). They mainly are *early-type* galaxies that no longer have ongoing star formation and have similarly evolved passively. To complete the sample of cluster members, bluer galaxies below the red sequence require close attention, because they might be infalling galaxies or galaxies with a high

star formation rate that truly belong to the cluster.

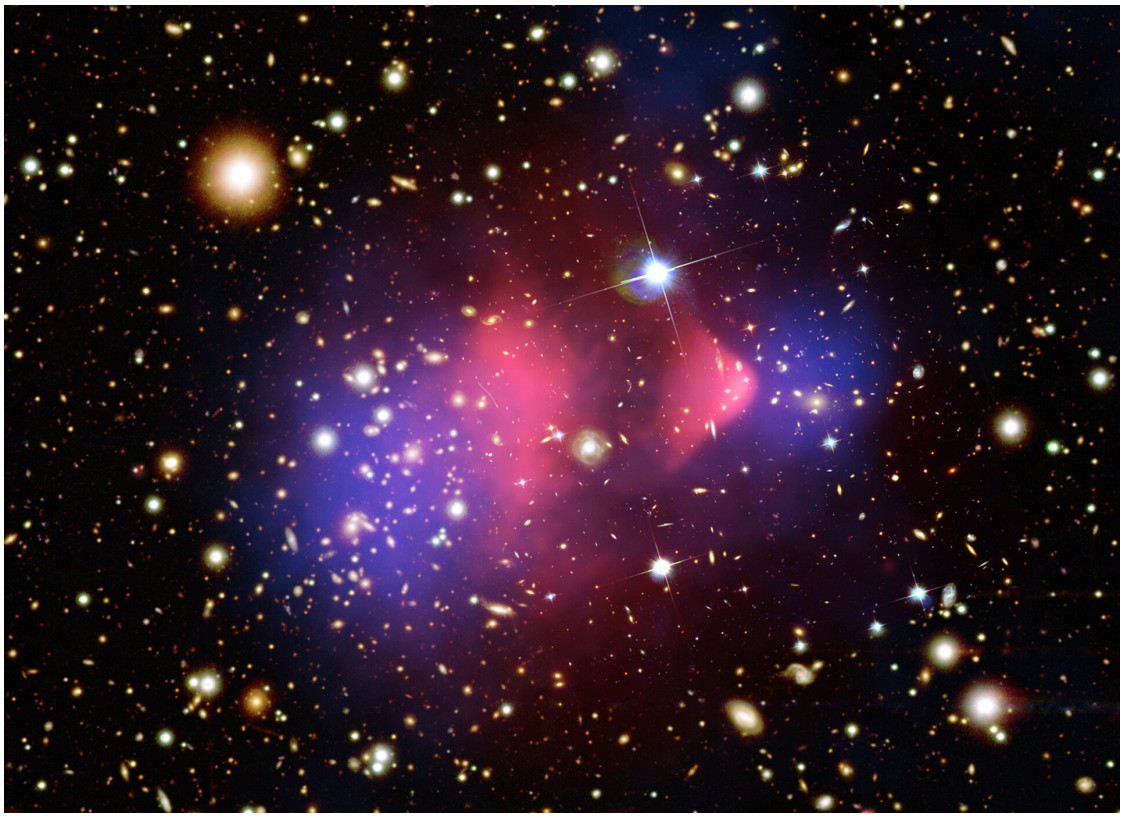

Figure 1.3: Multiband image of the Bullet Cluster, showing in pink the intracluster hot gas and in blue the dark matter halos of the two galaxy clusters. The yellowish and bluish light dots are the galaxies in the space. CREDIT: X-ray: NASA/CXC/CfA/M.Markevitch, Optical and lensing map: NASA/STScI, Magellan/U.Arizona/D.Clowe, Lensing map: ESO WFI

An example of such a galaxy cluster is shown in Figure 1.3, known as the Bullet Cluster. We can see two galaxy clusters that have collided with one another. The Bullet Cluster is very well known for providing direct evidence of both regular and dark matter, whose distributions can be clearly distinguished is pink and blue, respectively.

Galaxy clusters can be relaxed or undergoing mergers, like the Bullet Cluster. Relaxed clusters are in dynamical equilibrium and have a well-defined morphology with a central, brighter galaxy. Mergers happen when two clusters are very close to each other and, due to gravitational forces, they end up becoming a single one.

Dark Matter

The main component of a galaxy cluster is dark matter. Dark matter cannot be seen, but its existence can be inferred. A cluster merger is a very good laboratory to do so. The hot gas in the merging clusters slows down during the interaction, due to gravitational forces on a collisional fluid, while galaxies and dark matter remain undisturbed. Since the gas represents the biggest part of the baryonic matter, we would expect the potential well of the lens to be deeper where the gas is concentrated; however, it matches the position of the galaxies (see Figure 1.3), indicating

the existence of invisible mass in that region.

Another piece of evidence is that, the mass of a galaxy cluster can be estimated from the luminosity of its cluster members using the M/L ratio. The expected velocity of the clusters for this estimated mass is lower than the one actually observed, to the point that galaxies moving at the estimated velocity would escape the cluster. This suggests the mass in a cluster is larger than initially thought, indicating for the first time the existence of what we call dark matter.

Later it was discovered that the hot gas in a galaxy cluster emits X-rays. The hotter the gas, the deeper the potential well is, to keep the gas locked in. Again, mass estimates from X-ray emission suggest the presence of dark matter in galaxy clusters.

A third method that indicates the existence of dark matter is gravitational lensing, which depends on the total mass of the lens (a galaxy cluster for instance) regardless of its nature or dynamical state. The deflection observed does not agree with the expectations of the mass of galaxies and hot gas; therefore, there must be a third component that cannot be seen. Given that strong gravitational lensing is the main focus of this work, we detail in the following Section the theoretical framework needed to implement our analysis.

1.3 Gravitational lensing

Gravitational lensing is a phenomenon that occurs when light is deflected by a massive object, like a galaxy or a cluster, in its path to the observer; and the path is thus curved. As a result of gravitational lensing, very distant objects can be observed, thanks to the induced magnification. A single background source can project several images of itself. These images may be slightly different in shape, but always share the same colour, and can therefore be related to each other.

Multiple images are created as a consequence of the various ways in which the path of light is bent, in other words, the way in which space-time is curved. Depending on how many images are observed, their shape and their position, the total mass distribution of the lens can be determined. Light deflection in lensing does not distinguish between luminous or dark matter, and only depends on the total mass, regardless of its dynamical state.

One of the most important concepts in gravitational lensing is the deflection angle. It is used to measure the degree to which light is deviated from its original path. If a lens of mass M is located between the source and the observer, the total deflection angle, $\hat{\boldsymbol{\alpha}}$, is

$$\hat{\boldsymbol{\alpha}} = \frac{4GM}{c^2\boldsymbol{\xi}}, \tag{1.15}$$

where c is the speed of light and $\boldsymbol{\xi}$ is the impact parameter.

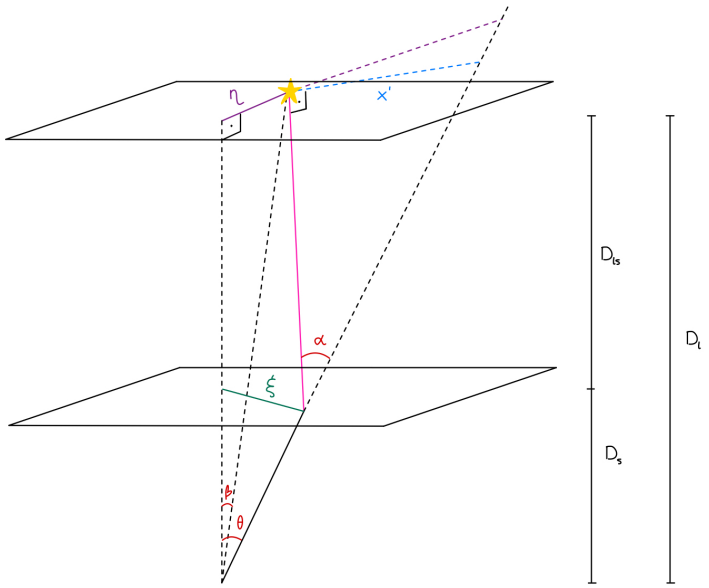

Figure 1.4: Sketch of a typical lensing configuration. The source plane is on the top, image plane in the middle, observer at the bottom. The angular diameter distances between the lens, the observer and the sources are shown on the right.

In Figure 1.4, $\boldsymbol{\eta}$ and $\boldsymbol{\xi}$ are two-dimensional vectors representing the real and observed positions of the source on the source and lens planes, respectively. Regarding the angles, $\boldsymbol{\beta}$ is the angular position on the source plane, $\boldsymbol{\theta}$ the angular position on the image plane and $\boldsymbol{\alpha}$ is the deflection angle: the difference between the actual path of light and the one observed. D_l, D_s and D_ls are the angular-diameter distances between the observer and the lens; the observer and the source; and the lens and the source, respectively. Even though the trajectory of light is simplified in Figure 1.4 as a straight line, it is actually curved. Lensed objects follow the lens equation, that can be derived from simple geometrical considerations such as

$$\tan\boldsymbol{\theta}\cdot D_\mathrm{s} = \frac{\frac{\boldsymbol{\xi}\cdot D_\mathrm{s}}{h}}{\frac{D_\mathrm{s}}{h}} = \boldsymbol{\xi} \approx \boldsymbol{\theta}\cdot D_\mathrm{s}, \tag{1.16}$$

$$\tan\boldsymbol{\beta}\cdot D_\mathrm{s} = \frac{\frac{\boldsymbol{\eta}\cdot D_\mathrm{s}}{h'}}{\frac{D_\mathrm{s}}{h'}} = \boldsymbol{\eta} \approx \boldsymbol{\beta}\cdot D_\mathrm{s}, \tag{1.17}$$

$$\tan\hat{\boldsymbol{\alpha}}\cdot D_\mathrm{ls} = \frac{\frac{\boldsymbol{x'}\cdot D_\mathrm{ls}}{h''}}{\frac{D_\mathrm{ls}}{h''}} = \boldsymbol{x'} \approx \hat{\boldsymbol{\alpha}}\cdot D_\mathrm{ls}. \tag{1.18}$$

Since the image of the source is seen at the position resulting from the vector sum of the original position and the deflection,

$$\boldsymbol{\xi} = \boldsymbol{x'} + \boldsymbol{\eta}, \tag{1.19}$$

which, in angular positions can be translated as

$$\boldsymbol{\theta}\cdot D_\mathrm{s} = \boldsymbol{\beta}\cdot D_\mathrm{s} + \hat{\boldsymbol{\alpha}} D_\mathrm{ls}, \tag{1.20}$$

and that scaled by an $1/D_\mathrm{s}$ factor can be written as

$$\boldsymbol{\theta} = \boldsymbol{\beta} + \hat{\boldsymbol{\alpha}}\frac{D_\mathrm{ls}}{D_\mathrm{s}} = \boldsymbol{\beta} + \boldsymbol{\alpha}; \tag{1.21}$$

if $\boldsymbol{\alpha} = \hat{\boldsymbol{\alpha}} D_{\rm ls}/D_{\rm s}$.

The deflection angle can also be expressed as a function of the lensing potential of the lens, ϕ. This is as follows:

$$\boldsymbol{\alpha} = \nabla\phi(\boldsymbol{\theta}, \boldsymbol{\beta}). \tag{1.22}$$

1.3.1 Time delays

Time delay is the additional time it takes for light to reach the observer in the presence of a gravitational lens. To be able to measure time delays, a variable source, like a supernova or a quasar, is required. The scarcity of these phenomena combined with strong gravitational lensing, is what currently holds major breakthroughs in this field. Time delay can be expressed in terms of distance and velocity, specifically speed of light, c, as follows:

$$\tau(\boldsymbol{\theta}) = \frac{1+z_{\rm l}}{c}\frac{D_{\rm l}D_{\rm s}}{D_{\rm ls}}\left[\frac{1}{2}(\boldsymbol{\theta}-\boldsymbol{\beta})^2 - \psi(\boldsymbol{\theta})\right], \tag{1.23}$$

where τ is the time delay itself, $z_{\rm l}$ is the redshift of the lens, and ψ is the lens Shapiro potential. $\boldsymbol{\theta}$, $D_{\rm l}$, $D_{\rm s}$, $D_{\rm ls}$ and $\boldsymbol{\beta}$ are as previously described.

In Eq. (1.23) two different terms can be identified inside the brackets. The term on the left is the geometrical contribution of the lens to the time delay, which arises due to the different path light follows. The term on the right represents the gravitational potential delay, which, according to the Shapiro effect, accounts for the slowdown light experiences when going through a gravitational lens.

Time delay thus depends on the so-called time-delay distance, $D_{\Delta t}$, which is a ratio of three angular diameter distances. $D_{\Delta t}$ is included in the first term of Eq. (1.23): $D_{\Delta t} = (1+z_{\rm l})D_{\rm l}D_{\rm s}/D_{\rm ls}$.

It is important to distinguish between time delay excess and relative time delay. Time delay excess is what has been described as 'time delay': the additional time it takes for light to reach an observer due to geometrical and gravitational effects. Whereas time delay excess cannot be directly measured (it is impossible to know how long it would take for light to travel in a straight line); relative time delay can, and it is what we effectively call time delay. As its own name suggests, it is the difference in arrival times between two multiple images.

To measure relative time delays, brightness variations of the variable object are monitored. A very similar pattern is expected from all the multiple images, but happening at different times and probably different magnitudes (the latter can be overlooked), as further described in the next Chapters. The time variation needed to match both light curves is the relative time delay. Were there two multiple images, each with a time delay excess τ_i and τ_j, the relative time delay would be the difference between them, bearing in mind that the same lens-source system is represented by the same time delay distance. It can be written as follows:

$$\Delta t_{i,j} = \frac{D_{\Delta t}}{c}\left[\frac{1}{2}(\boldsymbol{\theta}_i-\boldsymbol{\beta}_i)^2 - \psi(\boldsymbol{\theta}_i) - \frac{1}{2}(\boldsymbol{\theta}_j-\boldsymbol{\beta}_j)^2 + \psi(\boldsymbol{\theta}_j)\right]. \tag{1.24}$$

Time delay is thus sensitive to the values of the cosmological parameters, such as the Hubble constant, H_0. Time delay distance, $D_{\Delta t}$ is inversely proportional to H_0 and, consequently, so is it $\tau(\boldsymbol{\theta}, \boldsymbol{\beta})$.

1.3.2 Simple mass-density distributions

A good lens model can be described as a combination of different mass distributions that simulate each component of the system. There are several possible options, but all of them are derived from two basic mass-density distributions: point-mass and singular isothermal sphere, both of which are axially symmetric.

If a mass distribution is axially symmetric, it means it is not relevant whether the positions of mass distributions are summed as vectors or as scalars. The centre of the lens is located at the centre of symmetry and all the parameters in the lens equation, Eq. (1.21), are collinear. Therefore, equations become one-dimensional. This kind of lens has a bounded deflection angle, $|\alpha| \leq \alpha_{\max}$. If $\theta \approx \beta$ a single multiple image is projected. A solution to the lens equation represents a possible multiple image. Therefore, studying the derivatives of the lens equations and finding local maximums and minimums, the amount of multiple images can be determined. Another possibility for multiple images arises from the mean surface mass density, $\kappa(\theta) > 1/2$. Deflection angles in axisymmetric lenses can be described as

$$\beta = \theta - \alpha(\theta) = \theta - \frac{m(\theta)}{\theta}. \tag{1.25}$$

For simple mass distributions, multiple images are mostly found at the Einstein radius distance, θ_{E}, that marks the area where light is bent enough to form multiple images:

$$\theta_{\mathrm{E}} = \sqrt{\frac{D_{\mathrm{ls}}}{D_{\mathrm{s}} D_{\mathrm{l}}} \cdot \frac{4GM(<\theta_{\mathrm{E}})}{c^2}} \tag{1.26}$$

If the source and the lens are perfectly aligned, a rare phenomenon takes place: the Einstein ring. Instead of several multiple images, a single circle around the lens is observed.

The most basic mass-density distribution is the **point-mass lens**, in which mass, instead of being distributed along the space, is concentrated in a single point. Therefore, all the mass is within the Einstein radius and the term $M(<\theta_{\mathrm{E}})$ of Eq. (1.26) can be simplified as M, making $m(\theta) = \theta_{\mathrm{E}}^2$. Point-mass lenses are mainly used in microlensing, a kind of lensing that is caused by less massive objects and that allows for this approximation.

Another simple mass-density distribution is the **Singular Isothermal Sphere**, or SIS, which is a spherically symmetric lens and has a one-dimensional velocity dispersion, σ_0. It abides by Virial equilibrium and, as a consequence, the model does not work properly near the centre, when $r \to 0$. A large cut-off radius, r_{cut} is needed to avoid mass divergence at large radii and to ensure the flatness of curves as far as they can be seen. For SIS models the angular deflection can be expressed as

$$\alpha = 4\pi \left(\frac{\sigma_0}{c}\right)^2 \frac{D_{\mathrm{ls}}}{D_{\mathrm{s}}} \equiv \theta_{\mathrm{E}}, \tag{1.27}$$

not depending on θ. The lens equation can be expressed as follows:

$$\beta = \theta - \theta_{\mathrm{E}} \frac{\theta}{|\theta|}. \tag{1.28}$$

If $|\beta| < \theta_{\mathrm{E}}$ multiple images are observed, whereas if $\beta = 0$, it is an Einstein ring.

Strong lensing is caused by galaxy clusters and, so, a combination of mass-density distributions is required. Not only that, but also more complex models are needed to get good enough results. In the particular case of SDSS J1029+2623 dark matter halos are considered non-isothermal ellipsoids, foreground and background galaxies are Jaffe spheres, and the external shear is indeed a shear. These will be explained in Chapter 2.

1.3.3 Cosmography with lens galaxy clusters

Gravitational lensing in galaxy clusters can also be exploited to measure the values of other cosmological parameters, such as the matter density Ω_m; the equation of state of dark energy, and particularly the present-day value for the dark energy parameter, w_0, as is later explored in this work.

Multiple background sources at different redshifts, as happens in galaxy clusters, help mitigate the effect of degeneracies between the effect of the cosmology and the effect of the mass of the lenses. If there are several sources, the lens equation (Eq (1.21)) can be applied to each of them. Since $\boldsymbol{\alpha}$ depends on the total lens potential, which is the same for all the background sources, having multiple angular diameter distances for a single lens potential allows for tighter constraints that help break the degeneracies between the lens potential and the cosmological model.

The following relation between angular diameter distances applies:

$$\boldsymbol{\Xi}_{i,j} \equiv \frac{D_{\mathrm{l},i} D_{\mathrm{s},j}}{D_{\mathrm{l},j} D_{\mathrm{s},i}}, \tag{1.29}$$

where $\boldsymbol{\Xi}$ is the distance ratio. Eq- (1.29) shows that strong lensing is sensitive to H_0 (which scales inversely with the angular diameter distance), and can be used to constrain certain cosmological parameters.

Ω_k remains poorly constrained with strong lensing due to the high statistical uncertainties, even though the values are consistent with other probes. w shows some sensitivity on the cosmological model, and Ω_m is the most sensitive parameter of all and, therefore, the one with the tightest constraints. The more free cosmological parameters we leave in the model, the higher the statistical uncertainties are, which is somehow expected due to possible degeneracies.

These constraints can be improved when the results are combined with those obtained from other cosmological probes. In order to constrain more tightly all the cosmological parameters, we should no longer rely on improvements on current methods. Independent probes that work under different assumptions need to be developed. This way, new systematics will be addressed and results will improve.

1.3.4 State-of-the-art

Strong lensing is now gaining a lot of importance in cosmography studies. It has already been mentioned that Refsdal was the first to propose using the lensing of variable sources to measure time delay and hence the Hubble constant. He leaned towards supernovae, but it was soon realised that lensed quasars were a much more suitable phenomenon for this purpose. This is because quasars are a constant source of light and by observing them for long periods of time they eventually vary. Meanwhile, supernovae can happen at any time and place in the Universe, so it is harder to find

them lensed.

In one of the latest investigations on the strong lensing of a quasar, Grillo *et al.* (2024) studied the value of the Hubble constant for different cosmological models and compared gravitational lensing with other probes of MACS J1149+2223. It was concluded that strong lensing can provide very precise values for H_0 if the system has enough multiple images (89 from 28 different sources in this system). Another positive aspect of strong lensing over other probes like the Cosmic Microwave Background (CMB) is that with lensing, the cosmological parameters can also be calculated, opening the door to the idea of different cosmologies.

Similar results were reached by Wong *et al.* (2020), where six lensed quasars were analysed by the Hubble observations of lensed quasars and galaxies with optical wavelength, H0LiCOW, (H_0 Lenses in Cosmograil Wellspring): B1608+656, RXJ1131−1231, HE0435−1223, SDSS 1206+4332, WFI2033−4723, PG1115+080. Time delays were measured for the multiple images of the quasars, most of which are quads. Five out of the six lenses were monitored using COSMOGRAIL and the one left was monitored via radio observations. This article looked into the influence of microlensing and external convergence, finding that the presence of bright galaxies along the line of sight does affect the time delay and must be accounted for. In the end, different cosmological models were analysed for each quasar. They suggest a relationship between the redshift of the system and the estimation of H_0 that cannot be confirmed due to the little data available. Wong *et al.* (2020) introduces the idea of degeneracy between w and H_0 and combines the H0LiCOW modelling with others like Planck or Baryon Acoustic Oscillations, BAO. All in all, it is concluded that, providing H0LiCOW the most precise constraints, its results do not, nor seem to be going to, resolve the H_0 tension.

On the whole, current investigations are focusing on using different probes and analysing systematics that might affect the results. Once again, strong lensing is a promising tool for cosmography studies. While the use of quasars is more widely spread, results obtained from supernovae are expected to be more precise. This is because, even though we do not know when or where they will take place, we know how they behave, facilitating their analyses. Improvements in telescopes and space surveys that lead to a broader sample of lensed supernovae and quasars may turn out to be what we need to put an end to the H_0 tension and finally find the physics that describe the Universe.

1.4 The Hubble constant

The Hubble constant gets its name from Edwin Hubble, the first person to provide evidence of the expansion of the Universe, although this phenomenon was first noticed by Georges Lemaître. Hubble measured the redshifts of spectral lines that had been previously measured and realised that the further an object is, the faster it moves away, showing this proportionality a linear behaviour. Therefore, that is what the Hubble constant determines: the rate of expansion of the Universe comparing the recession velocity of a galaxy with its distance.

All of the measurements done throughout these years were related to the distance of galaxies estimated with the cosmic distance ladder. In Refsdal (1964) it was proposed for the first time the possibility of using time variable sources to measure H_0 using time delays. These sources can either be supernovae (as was initially intended) or quasars (which are more common in strong

lensing).

In the last 15 years, great improvements have been made towards the Hubble constant. Planck was a space mission that operated between 2009 and 2013. The mission gathered high-precision data to confirm the Big Bang Theory and detect the Cosmic Microwave Background, CMB. The CMB data together with other cosmological assumptions like the Cold Dark Matter model, flat ΛCDM, cosmology (see Chapter 4), inferred a value of the Hubble constant based on the early Universe. The high precision the Planck Space Mission guarantees for its measurements gives the $H_0 = 67.4 \pm 0.5$ km s^{-1} Mpc^{-1}. The issue with this value is that it cannot be directly measured, but rather inferred under the assumption of a given cosmological model.

When using strong lensing, as suggested by Refsdal (1964), we measure H_0 as well as other cosmological parameters, that are instead based on the late Universe. The currently accepted value from this technique is $H_0 = 73 \pm 1.8$ km s^{-1} Mpc^{-1}, that has been obtained by combining lensing with velocity dispersions. In addition, Type Ia Supernovae (SNe Ia) can be used as 'standard candles' to calibrate the magnitude-redshift relation and estimate the value of H_0. In Riess *et al.* (2022), a large sample of SNe Ia was analysed and a very consistent value for the late Universe is obtained, $H_0 = 73.04 \pm 1.04$ km s^{-1} Mpc^{-1}, entailing a $\sim 1\%$ precision. The 5σ discrepancy between the early and late Universe values of H_0 raises the Hubble constant tension.

The discrepancy may signal towards an issue with the cosmological model that would be solved with new physics, yet to be discovered. In order to solve the tension, alternative cosmological probes have to be developed.

2 Parametric Strong Lensing Modelling of Galaxy Clusters

The strong lensing modelling of a galaxy cluster refers to the modelling of its total mass distribution, which acts as a lens. Strong lensing models of galaxy clusters can be divided into two main categories. The first one, and the one we have used in this work, is the parametric modelling. The second approach is often referred to as free-form, where the total mass distribution of the lens is divided in a grid, where each cell is a free parameter. Free-form modelling techniques have thus many more free parameters than parametric ones, often resulting in a negative number of degrees of freedom, since there are not enough observables. The free-form modelling can describe more complex structures, but we usually prefer parametric models that we can physically understand.

In this Chapter, we first present the different types of lensing observables (Section 2.1) to then focus on the adopted methodology to model the total mass distribution of the lens in Section 2.2 and the scaling relations in Section 2.3. Finally, the main characteristics of the `gravity.jl` (Lombardi 2024) software, which is used for the modelling, are presented in Section 2.4.

2.1 Observables

To model a lens system using strong lensing, one can use different types of observables, which depend on the underlying geometry of the Universe and on the total mass distribution of the lens. For our lens system, these observables are the positions of multiple images and the time delays between multiple images.

2.1.1 Positions of multiple images

The most common observables are the positions of multiple images. To find systems of multiple images, deep multi-band imaging from telescopes that are, if possible, space-based, is fundamental. In this way, we remove the blurriness created by the atmosphere of the Earth, enabling high-resolution observations of galaxy clusters. For many decades, a key facility has been the Hubble Space Telescope (HST), which observes over a wide range of wavelengths, from 115 to 2500 nm. More recently, the James Webb Space Telescope (JWST) is granting us with high-resolution imaging in the near-infrared and infrared, from 0.6 to 28.5 μm.

In high-resolution, deep, multi-band imaging we look for structures that have the same colour and a similar morphology, and that can be approximated to a possible multiple-image configuration (a lens equation solution). The accuracy in the positions of each multiple image position provided by the current instruments is of about $1-3$ pixels in each instrument, which means they can vary between the 0.03" and 0.4". The identification of possible multiple images is typically carried out

visually.

The findings from this primary inspection have to be, however, confirmed with spectroscopic data. A spectroscopic revolution has occurred with integral field units such as the Multi Unit Spectroscopic Explorer (MUSE), mounted on the Very Large Telescope (VLT) in Chile. Several multiple images are obtained from a single pointing of MUSE, in addition to tens of cluster members. MUSE has a field of view of $1' \times 1'$, which means the central region of a galaxy cluster, where the multiple images are located, can be imaged in a single shot. However, for extremely massive or merging clusters, more than one pointing is required. The wavelength range it spans goes from $\lambda = 4750$ Å to $\lambda = 9350$ Å, with a spectral resolution that reaches 2.4 Å. MUSE allows for spectroscopic measurements of redshifts of multiple images, that ranged from $z \sim 0.5$ to $z \sim 6$.

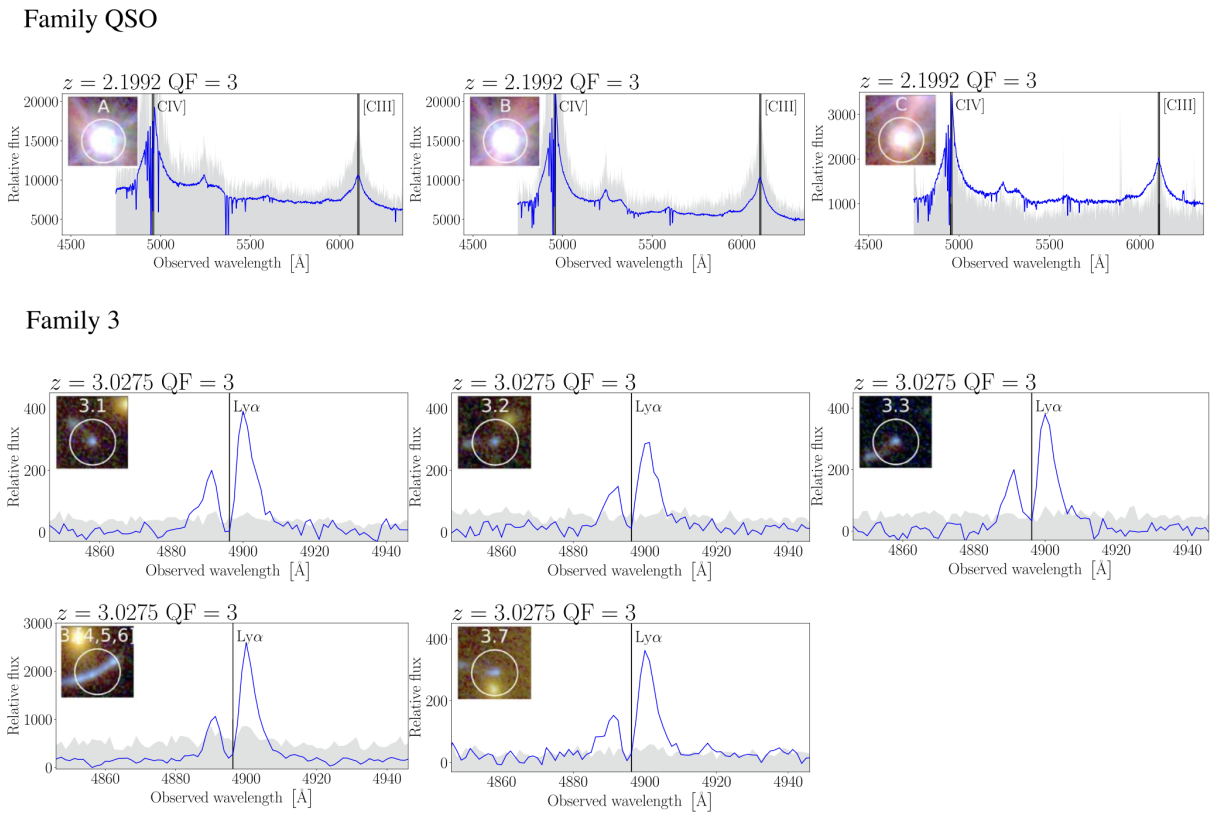

Figure 2.1: Spectra of the multiple images of the quasar system (top) and the System 3 (bottom) in SDSS J1029+2623. Figure adapted from Acebron *et al.* (2024).

In Figure 2.1 we can see how the multiple images of the same background source have the same emission lines, are located at the same redshifts and have the same colour and similar morphologies. The quality flag, QF, quantifies the reliability of the redshift measurement. QF = 3 means secure; QF = 2, likely and QF = 1, insecure. Using these data we can confirm whether they are multiple images or not. For both the quasar system, QSO, and Family 3 the similar morphologies and same colours can be seen at the top corner images.

2.1.2 Time delays

Strongly-lensed variable sources, like quasars or supernovae, not only provide observables through their positions. Light from the different paths reaches the observer at different times. A change in the flux happening in the source is seen at each multiple image at different times. This is what we call relative time delay, that follows Eq. (1.24).

To measure the time delays between multiple images, we need long-term observations that can last up to several years, depending on their cadence. One needs to monitor how the brightness of the different multiple images varies over time generally through ground-based, 1-2m class telescopes. The light curves of each of the multiple images of the variable source are then cross-correlated with each other, as they should show the same variability pattern at different moments. If both curves are superposed, the displacement in time of one of the multiple images light is the time delay. Effects like microlensing can introduce uncertainties when comparing two light curves. Low variability or sparse sampling are also important sources of uncertainty, where sparse sampling refers to an uneven curve that may have gaps and complicate the comparison.

2.1.3 Flux ratios

Using high-resolution photometric data, one can also measure the fluxes of the multiple images. The flux ratios between multiple images of the same source are related to the magnification. However, their estimates can be strongly affected by to phenomena such as microlensing or light contamination. Because of the possibly large uncertainties in their measurements, they are not used in this project, but are mentioned here just for completeness.

2.2 Mass density distributions

In parametric models, the total mass distribution of a galaxy cluster is decomposed into different mass components: the large-scale dark matter halo, the cluster members and the intracluster gas (see Chapter 1). The latter is usually included in the dark matter halo mass component because of strong model degeneracies without any prior and independent information on the mass distribution of the gas component.

2.2.1 Dark matter halos

To model the dark matter halos, we adopt non-singular isothermal ellipsoids (NIE). The potential is related to the deflection angle as shown in Eq. (1.22), and to the surface mass density as $\kappa(\boldsymbol{\theta}, \boldsymbol{\beta}) = \nabla^2\psi(\boldsymbol{\theta}, \boldsymbol{\beta})$. The 3D mass density profile of a NIE is:

$$\rho(r) = \frac{\rho_0}{1 + r^2/r_{\rm core}^2}, \tag{2.1}$$

where $\rho(r)$ is the 3D mass density at a given radius, r, ρ_0 is the central mass density and $r_{\rm core}$ is the core radius, characteristic of this mass-density distribution.

In `gravity.jl`, this mass density profile is defined using seven free parameters: the redshift, z, the position, $\boldsymbol{\theta} = (x, y)$, the core radius, $r_{\rm core}$, the velocity dispersion, σ_0, the position angle, θ, and the axis ratio $q = b/a$.

2.2.2 Cluster member galaxies

Cluster member galaxies are modelled with circular Jaffe mass density profiles, which are characterised by a core radius, $r_{\rm core}$ and a truncation radius, $r_{\rm cut}$. Jaffe spheres are three-dimensional density distributions that can be defined as

$$\rho(r) = \frac{\rho_0}{(1 + r^2/r_{\rm core}^2)(1 + r^2/r_{\rm cut})}. \tag{2.2}$$

From Eq. (2.2) we can conclude that there is a change of behaviour when the projected radius is smaller than the core radius, $r < r_{\rm core}$; between the core and the truncation radii, $r_{\rm core} < r < r_{\rm cut}$; or higher than the truncation radius, $r_{\rm cut} > r$. This matches the structure of elliptical galaxies, with a bright central bulk and a dusty halo. To define a Jaffe sphere, the free parameters required are z, $\boldsymbol{\theta}$, σ_0, $r_{\rm core}$ and $r_{\rm cut}$. To parametrise a Jaffe-like ellipsoid , the axis ratio and position angle would also be allowed to vary.

At $r \to \infty$, the total mass of a Jaffe-like profile can be defined as

$$M_{\rm tot} = \frac{\pi \sigma_0^2 r_{\rm cut}}{G}, \tag{2.3}$$

showing that the total mass of a cluster member is a function of its velocity dispersion and truncation radius.

2.2.3 External shear

The external shear component can account for external perturbations from nearby clusters or massive structures in the lens environment, for example. It is an additional term that is incorporated into the lens potential. It is characterised by the shear strength (amplitude), γ, and the position angle, θ. The external shear is frequently used to improve the reproduction of the observed positions of multiple images in galaxy clusters.

2.3 Scaling relations

Given that the number of multiple images in strong lensing galaxy clusters can range between tens to hundreds of multiple images, modelling each of the hundreds of member galaxies separately (with two free parameters each, σ_0 and $r_{\rm cut}$ as per Eq.(2.1)) would entail too many free parameters, and thus a negative number of degrees of freedom. The latter can be defined as

$$\mathrm{dof} = 2 \cdot N_{\rm mi} - \mathrm{N_{fp}}, \tag{2.4}$$

where $N_{\rm mi}$ is the number of multiple images, that is multiplied by a factor of 2 because each multiple image has two coordinates for its position, x and y. $N_{\rm fp}$ is the number of free parameters in the model. If dof is negative, it means that the model is overfitted and several models can predict the observed multiple images equally well.

To solve the issues that may arise from having too many free parameters, parametric lens models introduce two scaling relations that scale the truncation radius, $r_{\rm cut}$ and velocity dispersion, σ_0 of all the cluster members with their luminosity. These scaling relations are

$$\sigma_{0,i} = \sigma_0^{\rm ref} \left(\frac{L_i}{L^{\rm ref}} \right)^{\alpha}, \tag{2.5}$$

and

$$r_{{\rm cut},i} = r_{\rm cut}^{\rm ref} \left(\frac{L_i}{L^{\rm ref}} \right)^{\beta}. \tag{2.6}$$

In these equations, σ_0, $r_{\rm cut}$ and L refer to the velocity dispersion, truncation radius and luminosity of the i-th cluster members, respectively. Their respective reference values $\sigma_0^{\rm ref}$, $r_{\rm cut}^{\rm ref}$ and $L^{\rm ref}$ are reference values related to a given reference galaxy. The exponents α and β define the slopes of the two relations and one can adopt values that satisfy the fundamental plane of early-type galaxies, defined in Eq. (1.13). Thus, in parametric lens model, only two free parameters ($\sigma_0^{\rm ref}$ and $r_{\rm cut}^{\rm ref}$) are needed to model the total mass component associated with cluster member galaxies thanks to empirical scaling relations (Eq. (1.1), Eq. (1.12)).

2.4 Gravity.jl

`Gravity.jl` is a software in development that aims for better gravitational lensing models. `Gravity.jl` is developed in the `Julia` language, which is very similar to other programming languages such as `Python`. Unlike other software in the field, `Julia` uses just-in-time compilation techniques while looking like an interpreted language, which makes it fast and easy to use.

With `gravity.jl`, we can implement multiplane lensing, including information about foreground or background galaxies along the line of sight or multiple lens systems at different redshifts, that follow the lens equation

$$\boldsymbol{\beta} = \boldsymbol{\theta}_n(\boldsymbol{\theta}_1) = \boldsymbol{\theta}_1 - \sum_{i=1}^{n-1} \frac{D_{in}}{D_n} \hat{\boldsymbol{\alpha}}(\boldsymbol{\theta}_i, \boldsymbol{x}), \tag{2.7}$$

where $\boldsymbol{\theta}_n$, $\boldsymbol{\theta}_i$ and $\boldsymbol{\theta}_1$ are the positions of a multiple image in the n-th, i-th and first lens planes, respectively. D_{in} is the angular diameter distance between the i-th and n-th lens planes and D_n between the observer and the n-th plane. $\hat{\boldsymbol{\alpha}}(\boldsymbol{\theta}_i, \boldsymbol{\xi})$ is the deflection angle in the i-th plane caused by a model defined by $\boldsymbol{x}$ free parameters. This Equation is a generalisation of the single-plane lens equation presented in Chapter 1 Eq. (1.21).

Predictions are made using the Bayesian inference, which is based on Bayes's theorem. For a model M,

$$P(\boldsymbol{x}|D, M) = \frac{P(D|\boldsymbol{x}, M) P(\boldsymbol{x}|M)}{P(D|M)}, \tag{2.8}$$

where we are calculating the posterior distribution of the parameters $\boldsymbol{x}$, given the data D. It depends on $P(D|\boldsymbol{x}, M)$, the likelihood of the data given the parameters; and $P(\boldsymbol{x}|M)$, the priors of the parameters. The denominator $P(D|M)$ is known as Evidence, which is the probability of getting the data D given the assumed model M. Priors are assumptions that precede the inference and reflect our expectations. If no independent information is available, large, flat priors are assumed.

This software can work on the source plane or the image plane. Predictions on the source plane are computed faster because the posteriors returned are on the same plane as the priors provided.

The image plane, however, is the better-suited option for gravitational lensing, since it is the plane where we can actually have our observables and compare them to our predictions. The transformation from the source plane to the image plane is done through an inversion that, in the case of `gravity.jl`, used the Newton-Raphson method. This method essentially follows the following process: an initial model of parameter values of the results is made for the source plane; then the predicted positions of the multiple images can be used as starting points for the so-called 'simplified image plane', which is our final modelling scheme.

From `gravity.jl`, we do not only obtain the posterior probability distributions for our free parameters, but also the statistical uncertainties and all the necessary tools to compare different models. From the software, one can get the best-fit model, that maximizes the Log Evidence and the inferred parameters to model that posterior. To assess the goodness of our models we use four statistical indicators or figures of merit: rms, $\chi^2_{\rm red,x}$, $\chi^2_{\rm ,td}$ and Log Evidence. rms stands for root mean square and measures the offset between the observed and model-predicted positions of the multiple images, given a set of model parameters, $\boldsymbol{x}$. It abides by the following expression for a system with n multiple images:

$$\text{rms} = \sqrt{\frac{1}{N}\sum_{i=1}^{N} ||\boldsymbol{\theta}^i_{\rm obs} - \boldsymbol{\theta}^i_{\rm pred}||^2}, \tag{2.9}$$

being $\boldsymbol{\theta}^i_{\rm obs}$ and $\boldsymbol{\theta}^i_{\rm pred}$ the observed and model-predicted position vectors, respectively. N is the total number of multiple images in the system. Similar to the rms, the total chi-square function is χ^2, accounts for the differences between observed and model-predicted observables. In this work, we have considered two types of observables: the positions of multiple images and the time delays between pairs of multiple images of a background, variable source. Thus, the total chi-square function is defined as the sum of two terms, $\chi^2_{\rm ,x}$ and $\chi^2_{\rm ,td}$. The first one refers to the positions of the multiple images and has the following expression:

$$\chi^2_{\rm ,x} = \sum_{j=1}^{n} \frac{|\boldsymbol{\theta}^j_{\rm obs} - \boldsymbol{\theta}^i_{\rm pred}|^2}{\sigma_j^2}. \tag{2.10}$$

Here, $\boldsymbol{x}^j_{\rm obs}$ is the observed position of a multiple image, $\boldsymbol{\theta}^i_{\rm pred}$ is the model-predicted value of said multiple image, and σ_j is the uncertainty for the observed position of the multiple image. To calculate the associated reduced $\chi^2_{\rm red,x}$, we divide the value obtained from Eq. (2.10) by the number of degrees of freedom in the model, using Eq. (2.4). We expect a value of ≈ 1, which indicates that the uncertainties have been properly estimated.

The second χ^2 term is related to the goodness of a model in estimating the measured time delays, which is defined as

$$\chi^2_{\rm ,td} = \sum_{j=1}^{n} \frac{|t^j_{\rm obs} - t^j_{\rm pred}|^2}{\sigma_j^2}. \tag{2.11}$$

Here, following the same logic as before, $t^j_{\rm obs}$ represents the measured time delays and $t^j_{\rm pred}$ is the model-predicted time delay for the j-th multiple image. Again, σ_j is the uncertainty for the measured time delay.

The last indicator, Log Evidence, is the most complete one. It gives the goodness of a model according to the multiple images, the time delays, and the complexity of the model.

Posteriors in the models are in the form of Markov chain Monte Carlo (MCMC).Based on combining probability distributions of the free parameters within the provided priors. These combinations are repeated up to thousands of times, searching for the most likely combination. Particularly, MCMC examines the probability of a combination of a set of parameters and only accepts it if the likelihood is higher than the previously accepted point; otherwise, it is discarded. The posteriors we obtain are probability density functions from which we can obtain other statistical parameters like the mean, median, standard deviation 1σ errors, or the best-fit parameter values.

3 SDSS J1029+2623

3.1 Discovery

In this work, we present an extensive lensing analysis of SDSS J1029+2623, in 2006 using the Sloan Digital Sky Survey, SDSS (Inada *et al.* 2006). Its name reflects the coordinates where it is located. SDSS J1029+2623 is a unique and rare system in our Universe as one of the few currently known lens clusters with multiple images of a background ($z_s = 2.199$) quasar with a measured time delay. As detailed in the previous Chapters, this opens a window for using this system as a cosmological probe. The relevance of this object resides in the large angular separation between its quasar multiple images, caused by gravitational lensing from a foreground massive galaxy cluster. It is actually the system with one of the largest angular separations discovered so far and the second system of such characteristics chronologically found.

Initially, only two of the three multiple images of the quasar were observed, and no other sources with similar colours were found nearby. Their point-like morphology and colour, and identical redshift, suggested they could indeed be multiple images of a single background quasar, which were later labelled A and B. Both multiple images (A and B) are proven to have very similar emission/absorption patterns in their spectrum, supporting the multiple image theory (see Figure 2.1 in Chapter 2). The third image C, was confirmed two years later by Oguri *et al.* (2008), even though it had been discarded in previous investigations due to its fainter nature.

In this Chapter we first describe SDSS J1029+2623: we detail its main features and the most important information about the system in Section 3.2. Then, in Section 3.3 we present the telescopes and space missions that have provided photometric or spectroscopic data for the system and, finally, in Section 3.4, we comment on the results of the most recent strong lensing analysis of SDSS J1029+2623, which provides the reference strong lensing model for this work.

3.2 Main features and description

The cluster SDSS J1029+2623 is located at a redshift of $z = 0.588$, showing one of the most widely-separated strongly lensed quasars, with a maximum angular separation of ~ 22.5". The background source (the quasar) is located at a redshift of $z_s = 2.199$. These three multiple images are the most characteristic and interesting features of this cluster. The multiple images B and C are so close together and to the critical curve of the lens cluster (at the redshift of the quasar), that their brightness would be expected to appear similar, and significantly brighter than the multiple image A. However, this is not what we observe (see Figure 3.1) and is an effect called a flux ratio anomaly.

Indeed, the observed flux ratios between the multiple images of the quasar present an anomaly: the observed brightness differs from the model-predicted one or even, simple expectations from

strong lensing. The brightness of B and C are expected to be similar to each other and lower than that of A, due to their positions with respect to the critical line (where the magnification diverges). However, what we observe is that B and A have similar fluxes, that are higher than C, as can be clearly observed in Figure 3.1. This anomaly may be caused by microlensing or substructures in the dark matter halo, and is further discussed in Section 3.4. In the particular case of SDSS J1029+2623, the angular proximity of the hidden galaxy GX, marked in green in Figure 3.1, and located just where the multiple image C is, has a very important role in this anomaly. This galaxy is accounted for in this analysis.

X-ray observations from the Chandra telescope have shown that the flux anomaly is related to the pattern of absorption caused by external perturbations along the line of sight. Once this is accounted for in the models, the optical and radio flux ratios become highly consistent.

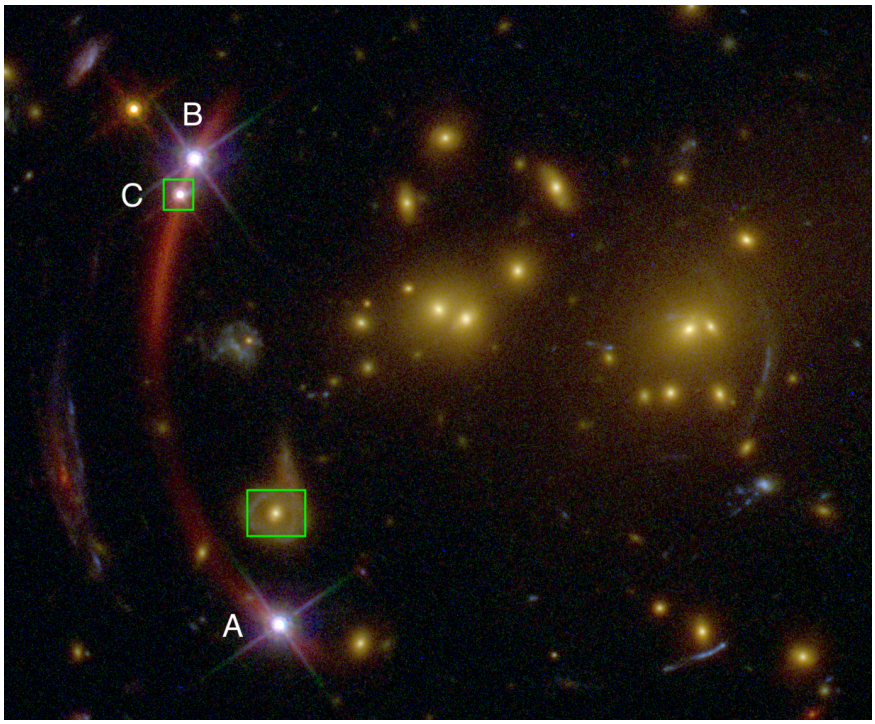

Figure 3.1: RGB image of the quasar SDSS J1029+2623 taken from the HST. The three multiple images of the quasar, labelled as A, B, and C, are marked. The galaxies that affect the flux of the multiple images of the quasar, SP and GX, are shown with green squares.

SDSS J1029+2623 is also of particular interest thanks to the measured time delay between two of the quasar multiple images. In Figure 3.2, we show the long-term monitoring of the quasar, lasting for 7 years, between 2005 and 2012. A great coincidence between the two light curves is clearly observed. This is how Fohlmeister *et al.* (2013) measured the relative time delay $\Delta t_{\rm AB} = 744 \pm 10$ days using long-exposure data obtained from the Fred Lawrence Whipple Observatory (FLWO) 1.2 m telescope and cross-correlating the two light-curves (see also Chapter 2).

This measurement clearly illustrates the time of arrivals of the light rays of each multiple image. The multiple image A is the first one to appear, followed by the multiple images B and C.

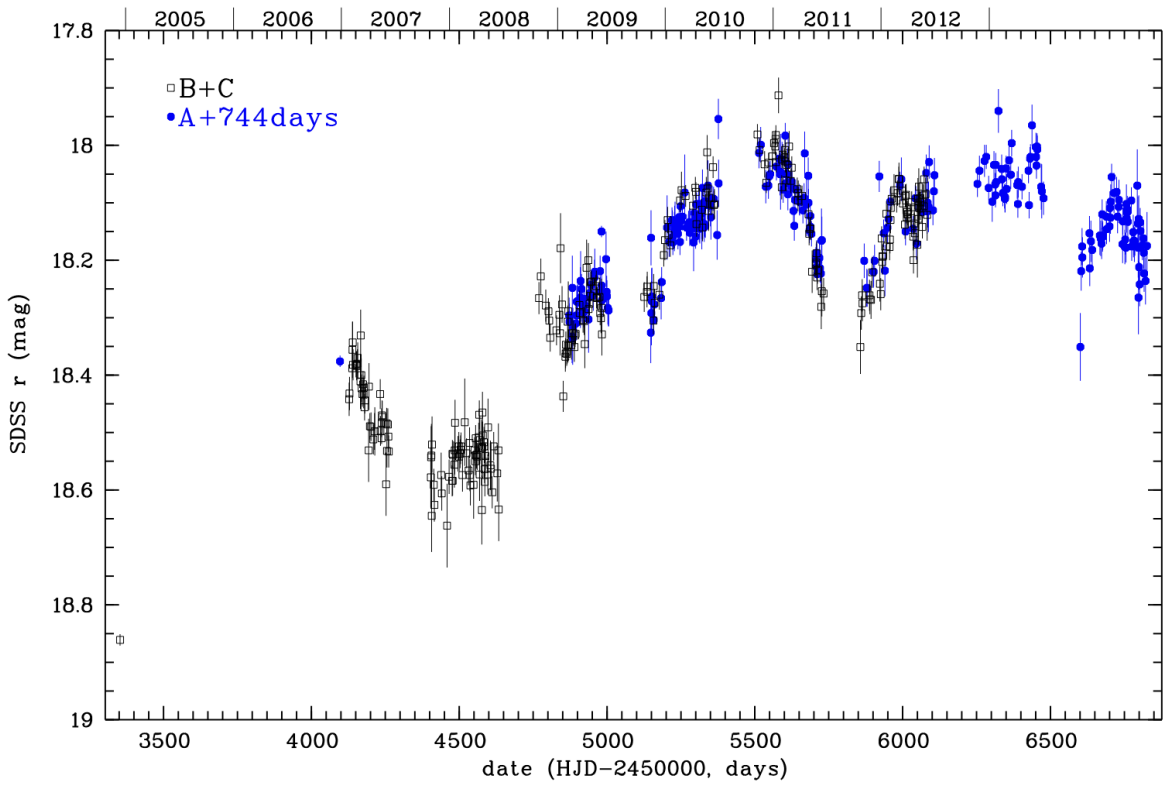

Figure 3.2: Light curve in the r band of the intrinsic variability of the multiple images A (blue) and B+C (black) from SDSS J1029+2623. The curve for A is displaced 744 days to match the curve of B+C and measure the time delay. Adapted from: Fohlmeister *et al.* (2013).

The strong lensing galaxy cluster is also noteworthy. There is numerous evidence that shows that the galaxy cluster is in an ongoing merger. The galaxy cluster shows a complex morphology that be confirmed through further X-ray analysis or other methods that might trace the mass profile in more detail. In fact, from the X-ray emission, it is observed how the mass-density profile is horizontally elongated, and has a smaller peak on the North-West region. The centre of mass of the hot gas does not match the centre of the dark matter halo overall, suggesting an ongoing or recent merger. Two sets of red galaxies are identified, each surrounding a brighter central galaxy. These are referred to as G1 and G2. Several tens of other galaxies in the field show similar redshifts and colours, as they lie on the red sequence, indicating they likely belong to the galaxy cluster.

3.3 Spectro-photometric data

As mentioned before, SDSS J1029+2623 was observed for the first time during a scan of the SDSS. It has been characterised over the years using photometric and spectroscopic data from different telescopes and observatories, as presented hereafter.

Deep images were obtained from the University of Hawaii 2.2 m (UH88) telescope, which provides photometric data. It was the UH88 telescope, along with long-term observations at FLWO 1.2 m

telescope, that provided evidence of the intrinsic and stochastic variability of the quasar multiple images, which is a common behaviour of quasars.

The HST has enabled a great leap forward in our characterisation of SDSS J1029+2623. It has already been mentioned that the HST is a high-resolution, multi-band instrument. It was essential to create complete catalogues of cluster members and multiple images for our lens system. The HST performed observations in different band through multiple orbits using the Advanced Camera for Surveys (ACS) and the Wide Field Camera 3 (WFC3).

The first spectroscopic data for the multiple images A and B were obtained using the Faint Object Camera And Spectrograph (FOCAS) in the Subaru telescope in 2006. Despite the bad seeing of the image, the large separation between the A and B facilitated the obtention of the spectra for each of them, which confirmed they are indeed multiple images of a quasar. The wavelength of these spectra ranges from $\lambda = 4700$ Å and $\lambda = 9400$ Å, very similar to that of MUSE.

Further spectroscopic data were obtained from the Keck I telescope. The confirmation of two components of G1 (G1a and G1b) was achieved, as well as the spectroscopic measurements of their redshifts and the relative velocity between G1b and G2.

The most precise and extensive spectroscopic measurements were obtained from MUSE. The observation consisted of 12 exposures of 1440 s, one of which failed. Spectroscopic redshifts of 127 objects of up to $z \sim 5$ of the objects detected with the HST have been measured with MUSE, using different apertures: one star, 12 foreground galaxies, 57 cluster members, 36 background and 21 multiple images galaxies (Acebron *et al.* 2022b).

3.4 State-of-the-strong-lensing analyses

The latest and most refined investigation on SDSS J1029+2623 can be found in Acebron *et al.* (2022b), where a complete and pure catalogue of cluster members and multiple images was built and included into the lens modelling. The redshifts of systems that had been only photometrically identified were spectroscopically confirmed for all background sources except for one; and a new high-redshift system has been detected thanks to the advances in the instruments.

A total of 26 multiple images have been securely identified, belonging to seven different sources, the quasar being one of them, spanning a wide redshift range, between 1.02 and 5.06, as shown in the right panel of Figure 3.3. However, the redshift of one of these objects does not have a spectroscopically confirmed redshift. Hence, it is treated as a free parameter with priors between $z = 1.18$ and $z = 3.18$.

The cluster has 83 identified members, within a F160W magnitude range 18 to 26 (see the left panel of Figure 3.3). The catalogue of cluster members contains 57 spectroscopically confirmed galaxies considered secure by their redshift QF; with six objects flagged as insecure. In addition, 20 extra cluster members have been selected outside of the MUSE field of view with the red sequence method by exploiting the available HST photometry. Looking at Figure 3.3 we can see that most of the cluster members lie between an F160W band of 21 and 23.

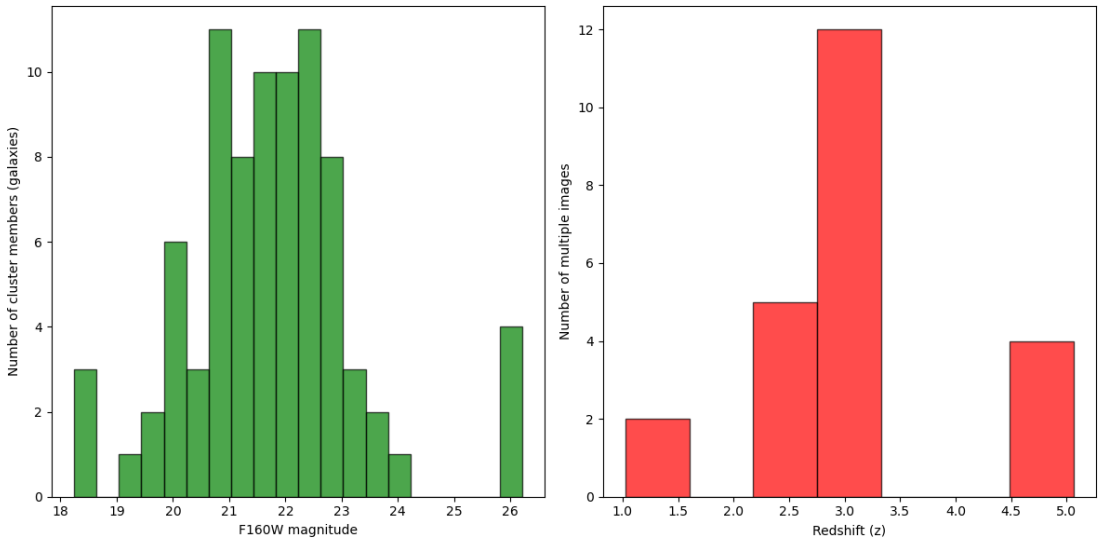

Figure 3.3: Characterisation of SDSS J1029+2623. The histogram on the left shows the classification of the cluster members for their F160W band. The graph on the right shows the amount of multiple images found at different redshift ranges.

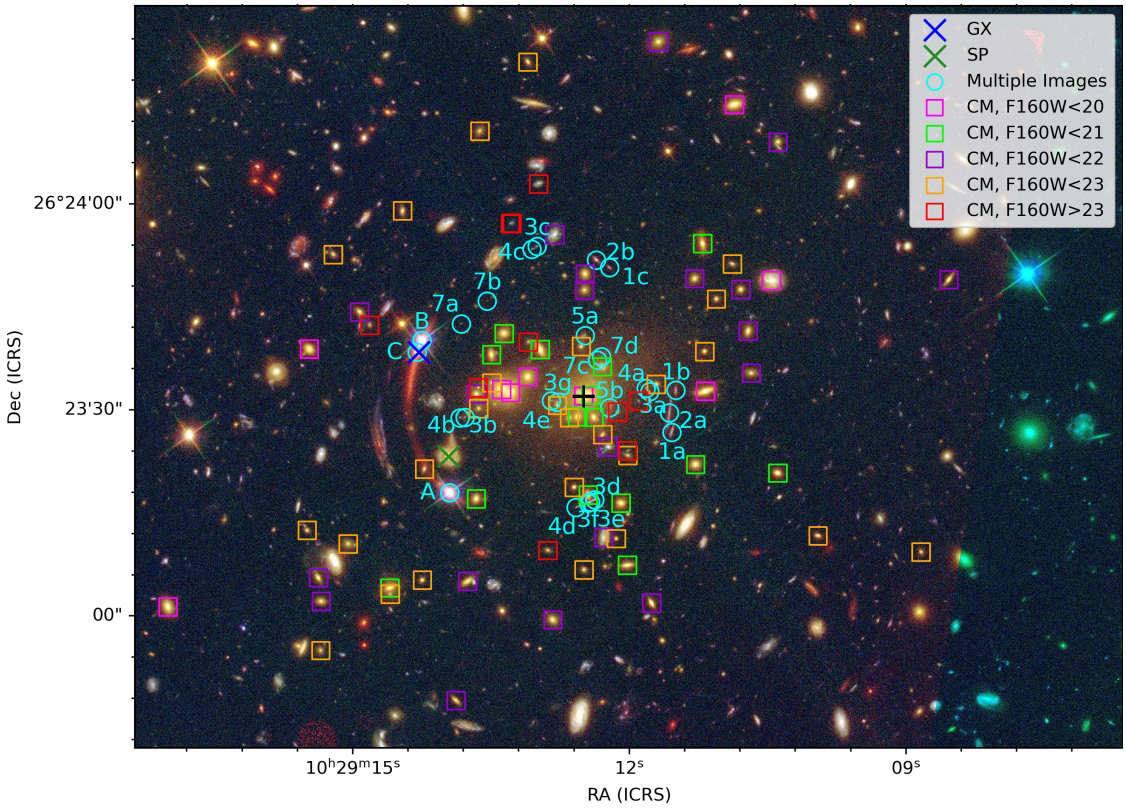

Figure 3.4: HST colour image presenting the different observables and mass components of SDSS J1029+2623. The cluster members (with different magnitude values in the F160W band) are shown in pink, green, purple orange and red; and multiple images, in cyan. The black cross indicates the centre of reference for our lens modelling. The blue and dark green crosses represent galaxies along the line of sight.

In Figure 3.4 we can see the cluster members and multiple images of our lens system. SP is a foreground galaxy found at a redshift $z_{\rm SP} = 0.511$, and GX is a background galaxy at $z_{\rm GX} = 0.6734$.

To run the lens model in Acebron *et al.* (2022b) the software `lenstool` was used. An equivalent version for `gravity.jl` was constructed and provided at the beginning of this work. The main components to model SDSS J1029+2623 used in Acebron *et al.* (2022b) are two dark matter haloes, that are parametrised using the NIE mass density profile (Chapter 2). Also, the background and foreground galaxies, GX and SP, are used in a multiplane environment in `gravity.jl` contrary to the `lenstool` model. The coefficients $\alpha = 0.39$ and $\beta = 0.42$ are used to satisfy the scaling relations from Chapter 1. Regarding the scaling relations from Chapter 2, reference values for the velocity dispersion, $\sigma_0 = 322^{+10}_{-9}$ kms^{-1} and a large, flat prior for the truncation radius, are considered. Finally, it also accounts for the effect of external factors with an external shear. The low rms value for the `lenstool` model, rms = 0.15", indicates the model-predicted values are very similar to the observed ones, hence, it is a good parametrisation.

The `Fiducial` model, the translated version of the `lenstool` model presented in Acebron *et al.* (2022b) and detailed above, is considered the reference model in the following. It is constructed under a fixed flat ΛCDM cosmological model. Going beyond the work in Acebron *et al.* (2022b) we include as an observable the measured time delay between the multiple images A and B, and leave H_0 as a free model parameter, optimised within a large, flat prior between 20 and 120 km s^{-1} Mpc^{-1}. The resulting median value of the H_0 distribution is $H_0 = 93.7 \pm 18.7$ km s^{-1} Mpc^{-1}. The obtained posterior probability distributions of a selected sample of model parameters are displayed in Figure 4.3.

In Figure 3.5 the different degeneracies among parameters in the `Fiducial` model can be appreciated. If two parameters are degenerate, one of them might change in favour of the other, but the eventual outcome remains unchanged. After thoroughly examining the corner plot with all the parameters in the model, these have been concluded to be the most degenerate ones. Perhaps the most obvious one is the position of the dark-matter haloes. The plots corresponding to the x and y coordinates of each dark matter halo (specially DM1) are correlated. This degeneracy means that the centre of the dark matter halos can be slightly displaced on one axis and compensated with the other one. Something similar happens to the velocity of dispersion, σ and the core radius $r_{\rm cut}$, as can be seen in Eq. (2.3). This is explained by the fact that, for example: a dark matter halo with lower $r_{\rm cut}$ has its mass more concentrated and, to achieve the same perturbation in space-time, less mass, and hence σ, is required. The velocity dispersion of both DM halos is also degenerate, because the velocity one lacks can be held by the other one. Finally, the H_0 value shows some kind of degeneracy with other model parameters. The same logic previously explained is followed: changes in position, σ_0 or $r_{\rm cut}$ alter the lensing potential, and in turn the path light follows to reach the observer in those time delays. Since the time delay is measured, both the mass and H_0 have to be adjusted to satisfy reality.

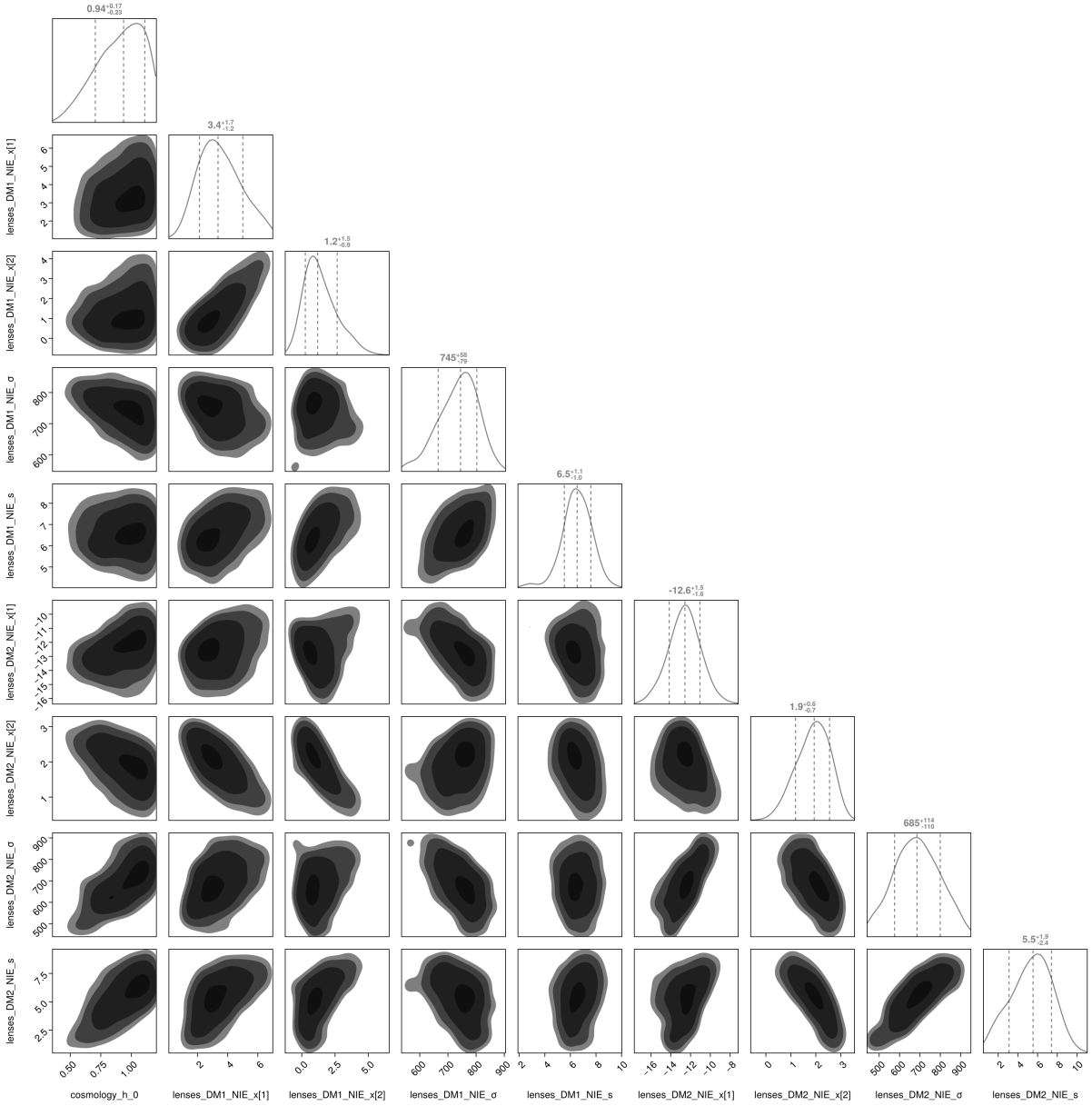

Figure 3.5: Marginalised probability distribution functions highlighting degeneracies between a selected sample of model for the `Fiducial` model of SDSS J1029+2623. The median values and 1σ uncertainties of these parameters are given at the top of each panel.

4 Results

This investigation aims to quantify the impact of systematic uncertainties in the time-delay cosmography technique, by analysing the strong lensing galaxy cluster SDSS J1029+2623, introduced in Chapter 3. This particular system is ideal to study the effect of systematics because of the measured time delay between the multiple images A and B (see Figure 3.4) and 23 additional multiple images from other sources at redshifts between 1.02 and 5.06. To do so, we have developed a set of several strong-lensing models of the galaxy cluster, making slight changes to each of them.

In the first part of this Chapter (Section 4.1), we describe each strong lensing model that we have studied. These models contain variations compared to the `Fiducial` model, which can be classified in four different categories: cluster members sample and modelling in Subsection 4.1.1, multiple images selections in Subsection 4.1.2, mass parametrisation in Subsection 4.1.3, and more general cosmological models in Subsection 4.1.4. After that, in Section 4.2, we present the H_0 inference with SDSS J1029+2623, while discussing the impact of different assumptions on cluster-scale time delay cosmography. In particular, four statistical estimators described in Chapter 2 are used to assess the goodness of each model: rms, $\chi^2_{,\mathrm{x}}$ (for positions), $\chi^2_{,\mathrm{td}}$ (for time delay) and Log Evidence. Finally, two additional tests are explored in Section 4.3 to assess the robustness of the results under different optimisation schemes with a software under development, as is `gravity.jl`.

4.1 Strong lensing models

4.1.1 Cluster members catalogue

In parametric models, the use of complete and pure catalogues of cluster members is crucial. The fiducial catalogue used for SDSS J1029+2623 contains 83 cluster members with F160W band magnitude values ranging from 18.14 to 26.22.

Magnitude truncation

The first potential source of a systematic bias that we have analysed is the completeness of the cluster members catalogue. In the following models, the F160W magnitude limit is truncated to subsequently brighter values, i.e. F160W$<$ 23, 22, 21 and 20.

- `F160W <23`: considers 73 cluster members (88% of the fiducial catalogue), highlighted in Figure 3.4 with all the squares except for the red ones.
- `F160W <22`: has 46 cluster members (55% of the fiducial catalogue), identified in purple, green and pink in Figure 3.4.

- `F160W <21`: contains 25 cluster member galaxies (30% of the fiducial catalogue), marked in green and pink in Figure 3.4.
- `F160W <20`: this model only includes 9 cluster members (11% of the fiducial catalogue), the brightest ones shown in Figure 3.4 with pink squares. Not all the multiple images are predicted in this model and, hence, it is too simple to be taken into account.

The exclusion of brighter galaxies in the lens model can deeply affect our final results, especially if the missing cluster members are located angularly close to multiple images, the expected impact being more important the brighter the missing galaxies are. In turn, this can affect the model-predicted time delays.

Constant M/L ratio

With this model, we can quantify the impact of the assumed M/L ratio of the cluster members. The `Constant M/L Ratio` model includes all the 83 cluster members from the `Fiducial` model. In the `Fiducial` model, the values given to α and β were such that M/L is consistent with the observed tilt of the Fundamental Plane relation. In this case, however, the ratio is set to be constant. To ensure a constant M/L, the exponent has to be 0, so, from Eq. (1.12) we get that

$$2\alpha + \beta - 1 = 0. \tag{4.1}$$

This equation differs from Eq. (1.13) on having a 0 instead of a 0.2, that ensures the ratio remains constant. A possible solution that satisfies this equation that will be used in this model, is $\alpha = 0.25$ and $\beta = 0.5$.

4.1.2 Multiple images catalogue

A lens model is characterised by its observables: the observed positions of multiple images. It is thus fundamental to determine which types of observables and information have a higher impact on time-delay cosmography, for example, high redshift sources or the lack of spectroscopic redshifts.

Redshift cut

One of the multiple image systems is located at a very high redshift, of $z_{\rm sys7} = 5.06$. As it can be appreciated in Figure 3.4, system 7 is formed by a set of four, very faint multiple images. A spectroscopic confirmation of these images can require very deep observations, which may not be available for all lensing clusters with strongly-lensed, time-varying sources.

To create the model `Redshift cut`, all the multiple images belonging to system 7 are removed from the multiple images catalogue. The cluster members and configuration file are the same as in the `Fiducial` model.

Optimised redshifts

As mentioned in Chapter 3, SDSS J1029+2623 hosts a system whose multiple images are not spectroscopically confirmed, system 1. However, these multiple images can be implemented in the model if the photometric information is enough to securely identify them. This motivates the verification of these assumptions.

To do so, instead of using the spectroscopic redshift of the lowest and highest redshift systems (systems 5 and 7) in the lens model, we leave them as free parameters, lifting the number up to 24. Their values are optimised within large, flat priors from 0.5 to 5.5 in both cases. The optimised redshift values are $z_{\rm sys5} = 1.05 \pm 0.02$ and $z_{\rm sys7} = 4.64 \pm 0.43$.

In Figure 4.1 we show the probability density functions of the optimised redshifts of systems 5 and 7 in the SDSS 1029+2623 multiple images catalogue. It can be appreciated how the expected values for both systems is within the 1σ confidence interval, with a relative error of 10% and 2% for systems 5 and 7, respectively. These results, especially in the latter case, offer a very good approximation. These findings showcase that strong gravitational lensing is an excellent technique to estimate the redshift values of the multiple images.

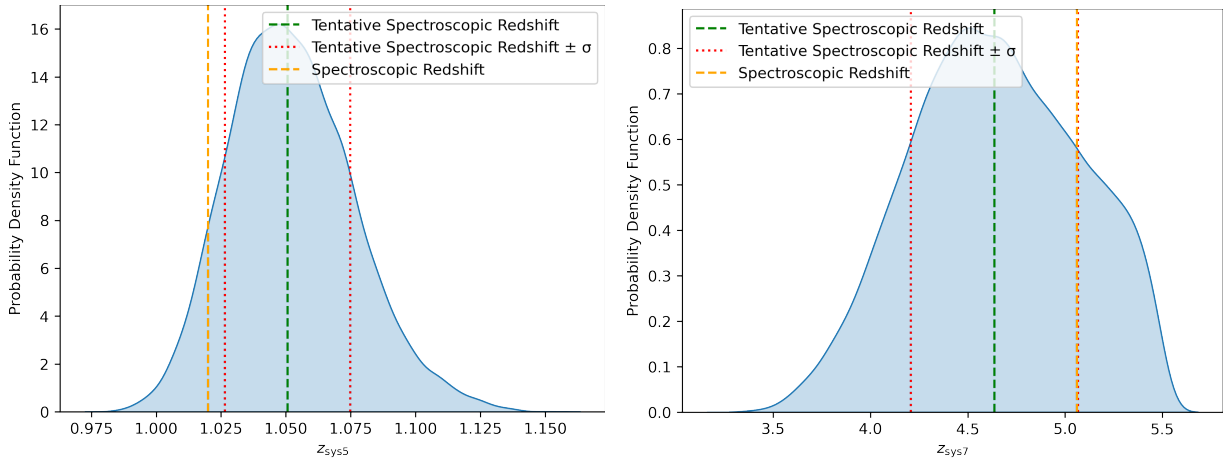

(a) (b)

Figure 4.1: Probability density functions of the optimised redshifts in the model `Optimised Redshift`. On the left, we show the PDF corresponding to system 5 with a tentative spectroscopic redshift $z_{\rm sys5} = 1.02$ and an optimised value of $z_{\rm sys5} = 1.05 \pm 0.02$. On the right we show the PDF of system 7, with a spectroscopic redshift $z_{\rm sys7} = 5.06$ and an optimised value of $z_{\rm sys7} = 4.6 \pm 0.4$.

4.1.3 Mass parametrisation

We remind that, from Eq. (1.24), it can be noted that the total error on the value of H_0 is approximately the sum in quadrature of the uncertainty of the time delay measurement (of 1.3% for the AB time delay estimate in SDSS J1029+2623) and that of the total mass parametrisation, which has been shown to dominate the total error budget. In this Section, we aim to assess possible systematic uncertainties arising from the different modelling assumptions.

Jaffe ellipses

In this model, the total mass density profile of the dark matter halos is changed from the NIE to the Jaffe Ellipse mass density profile. Whereas the Non-Singular Isothermal Ellipsoid is characterised by only a core radius, $r_{\rm core}$, and thus, a mass distribution that is not truncated, the Jaffe-like elliptical lens also needs a truncation radius, $r_{\rm cut}$. The `Jaffe Ellipses` model is thus slightly more complex. This model mainly aims at testing our inability at measuring with precision the value of $r_{\rm cut}$ in cluster-scale dark matter halos. This is because the truncation radius of strong

lensing clusters is very large, extending well beyond the region where the multiple images are located to provide any constraining power on the value of this parameter.

SIS

A model using the SIS (described in Chapter 1) mass density profile for the dark matter halos is also explored. The model has a Log Evidence of -415.89 driven by the lack of prediction of multiple images from the quasar and other systems, leading us to discard this model. It will not be taken into account for the cosmological analyses since the adopted mass distribution is too simple to realistically model such complex systems, as massive galaxy clusters are. This is expected from Eq. (1.27), which only has two possible solutions: $\theta_1 = \beta + \theta_E$ and $\theta_2 = \beta - \theta_E$. Hence, only systems with two multiple images could use this mass-density distribution, unlike our quasar system, which has three.

No external shear

This model removes the external shear term, that is used in the `Fiducial` model. The external shear is defined by two free parameters: the position angle θ, with priors between 0 and π; and the amplitude, γ, with priors between 0 and 0.1. It makes up for external perturbations, such as the unmodelled lens environment or a complex total mass distribution of the lens.

Other than that, the configuration file used is the same, as well as both the cluster members and multiple images catalogues. We find that it leads to the same outcome as the `F160W < 20`: not enough multiple images are predicted to consider the results as valid. We then conclude that this model is too simple.

Single plane

In Figure 3.4 are highlighted two objects, SP and GX, that are not part of the lensing cluster, but instead are located along the line of sight, angularly close to the multiple images of the quasar system. The `Single Plane` approximation assumes that these two galaxies have instead the same redshift as the lens, projecting all the mass along the line of sight into the lens plane. Again, the fiducial cluster members and multiple catalogues are used, and the only information that is changed in the configuration file is the redshift values of SP and GX.

Mass sheet

The `Mass Sheet` model introduces an additional convergence term. A mass sheet is a uniform mass distribution over which the lens model stands. The mass sheet transformation does not actually alter the observed positions, shapes, or magnification ratios of multiple images, but does affect the product of time delay and the Hubble constant, $H_0\Delta t$. In other words, the presence of a mass sheet can significantly affect the inferred value of H_0; however, changes will not be appreciated through the observables in our lens models. This is known as the mass-sheet degeneracy.

The mass-sheet degeneracy means that different mass density profiles make equally good predictions for the observables, which leads to high systematic uncertainties in time-delay cosmography at galaxy scales, as explained in Section 1.3. This problem loses relevance in cluster-scale systems, thanks to the presence of several sources at different redshifts, that make transformations like the

one in Eq. (4.2) less probable.

The mass sheet, κ, transforms $H_0\Delta t$ through the factor

$$\kappa_\lambda(\theta) \rightarrow \lambda\kappa(\theta) + (1-\lambda), \tag{4.2}$$

where λ is a constant. This will affect the Fermat potential, $\Delta\phi$. From Eq. (1.24) we can conclude that introducing a transformation in the convergence factor κ leads to a change $\lambda H_0\Delta t$.

By default, the mass sheet will be non-existent, i.e. $\kappa_\lambda(\theta) = 0$. In our cluster, the convergence factor κ is a new free parameter with large, flat priors from -0.5 to 0.5, with an inferred value of $\kappa = -0.40 \pm 0.10$.

4.1.4 Alternative cosmological models

Currently, the most widely accepted cosmological model is flat ΛCDM. This model stands on the Big Bang theory and the accelerating expansion of the Universe due to dark energy, set by the cosmological constant Λ. The term flat indicates there is no curvature and therefore the total energy density of the Universe is equal to, $\Omega = \Omega_m + \Omega_\Lambda = 1$, where $\Omega_m \approx 0.3$ and $\Omega_\Lambda \approx 0.7$. Ω_m represents the mean matter (both baryonic and dark) density in the Universe. Ω_Λ represents the dark energy density in the Universe. CDM stands for Cold Dark Matter and suggests the existence of non-baryonic matter whose particles can be considered colisionless. CDM represents in this cosmological model around 26% of the total energy density of the Universe, while the remaining 4% is the baryonic matter and, together with the non-baryonic matter, they make up $\Omega_m \approx 0.3$. Strong lensing is very sensitive to these parameters because they affect angular diameter distances (see Chapter 1). Different Ω_m or w values lead to changes in the positions of multiple images.

The catalogues in the `Fiducial` model are adopted.

Ω_m

In this model, the value of Ω_m is left free to vary within a large, flat prior between 0.01 and 1. By default, Ω_Λ will also vary to maintain the flat Universe. This means the Universe total energy density can either be constituted by just matter $\Omega_m = 1$ or just dark energy, $\Omega_m = 0.01$.

fwCDM

The model `fwCDM` does not only allow a different mass distribution of the Universe, but a truly different behaviour in which the dark energy equation is allowed to have a value different from $w = -1$. The optimised values of the cosmological parameters in this model are $w = -1.1 \pm 0.3$ and $\Omega_m = 0.4 \pm 0.3$.

Model	H_0 (km s^{-1} Mpc^{-1})	Relative Error (%)	rms (arcsec)	Log Evidence	DOF	$\chi^2_{,\mathrm{x}}$	$\chi^2_{,\mathrm{td}}$	$\chi^2_{\mathrm{red,x}}$
Fiducial	$93.7^{+30.4}_{-10.2}$	19.95	0.1630	−258.47	15	8.356	0.1362	0.5570
F160W<20	$91.9^{+30.3}_{-5.0}$	18.72	—	−256.75	15	—	—	—
F160W<21	$100.9^{+25.6}_{-7.6}$	16.59	0.1633	−257.52	15	8.313	0.3050	0.5542
F160W<22	$93.0^{+20.3}_{-21.8}$	22.74	0.1626	−257.91	15	8.821	0.1190	0.5881
F160W<23	$93.5^{+28.8}_{-10.7}$	19.65	0.1759	−258.90	15	8.093	0.7508	0.5395
Constant M/L ratio	$83.5^{+37.0}_{-5.2}$	23.54	0.1621	−264.45	15	8.175	0.2382	0.5450
Redshift cut	$85.8^{+21.7}_{-31.8}$	27.90	0.1949	−235.77	13	8.562	0.0776	0.6586
Optimised redshift	$91.0^{+19.1}_{-18.9}$	19.33	0.1407	−263.56	13	7.282	0.0173	0.5601
Jaffe ellipse	$95.0^{+18.3}_{-18.2}$	17.94	0.1932	−258.12	13	10.930	0.0923	0.8408
No external shear	$93.9^{+25.5}_{-13.7}$	19.07	—	−259.31	17	—	—	—
Single plane	$87.7^{+24.9}_{-26.5}$	26.79	0.1773	−256.10	15	11.435	0.4737	0.7623
Mass sheet	$95.5^{+16.1}_{-19.1}$	18.21	0.1528	−255.42	14	6.809	0.7084	0.4864
Ω_m	$94.4^{+20.6}_{-21.1}$	20.22	0.1804	−258.77	14	10.370	0.1430	0.7407
fwCDM	$96.4^{+21.3}_{-22.4}$	21.88	0.1719	−258.85	13	10.569	0.0214	0.8130
Combined	$93.7^{+17.6}_{-27.1}$	21.41	—	—	—	—	—	—

Table 4.1: Summary of the cosmological inference and statistics for each lens model. The H_0 values correspond to the median value of each model and the errors displayed are the 16^{th} and 84^{th} percentiles (or 1σ). Wherever a "—" is shown it means that the model is not accurate enough to predict all the multiple images and those values could not be calculated.

4.2 The influence of systematics in SDSS J1029+2623

4.2.1 Statistical estimators

In this Section, we look into the behaviour of the statistical parameters to determine the impact of the different systematics analysed in the strong lensing models.

The median H_0 values of all the models (except for `SIS`) above are reported in Table 4.1, along with the statistical parameters mentioned in the Introduction and described in Chapter 2. The values of Log Evidence quantify how well a model adjusts to the priors, accounting for the complexity of the model and how much said complexity improves the results. We note that, both in Table 4.1 and Figure 4.2, the $\chi^2_{\rm red}$ value should include both positional and time delay uncertainties. However, $\chi^2_{,\rm td}$ values are so small that their effect is negligible and, therefore, we only consider the positional $\chi^2_{,\rm x}$. Something worth remarking is that, according to Lombardi (2024), Log Evidence does not introduce a penalty if a model fails to predict some multiple images; it only does it if non-existent ones are found. As a result, the Log Evidence corresponding to the `Magnitude truncation F160W<20` and the `No external shear` models are not displayed on Figure 4.2 despite being available and provided by the software.

In Figure 4.2 we can see that, there are some models with better figures of merit than those of the `Fiducial` model, which is translated into lower values of rms or both χ^2 and higher values of Log Evidence (more positive). The `Optimised redshift` model clearly suggests an improvement over the `Fiducial` model in terms of rms and both χ^2, whereas the Log Evidence value is less positive. This can be explained by the higher flexibility provided by the two extra free parameters, that make better predictions at a complexity cost.

It is also noteworthy that the goodness of the models is not consistent in all four parameters. The pattern is similar in the first two graphs of Figure 4.2, which is somehow expected as they are both related to position. On the other hand, the time delay $\chi^2_{,\rm td}$ has some very different results, indicating that reproducing well the observed multiple images positions does not always imply reproducing well the measured time delays. Meanwhile, Log Evidence factors many other things, so its unique behaviour is not that surprising. A higher Log Evidence value suggests a better model and, for the most part, we can say that the cost of complexity and precision is more or less the same for all the analysed models, except for the `Redshift cut` model. In summary, we find that the systematics that we have studied do not have a significant impact on the overall goodness of the lens model.

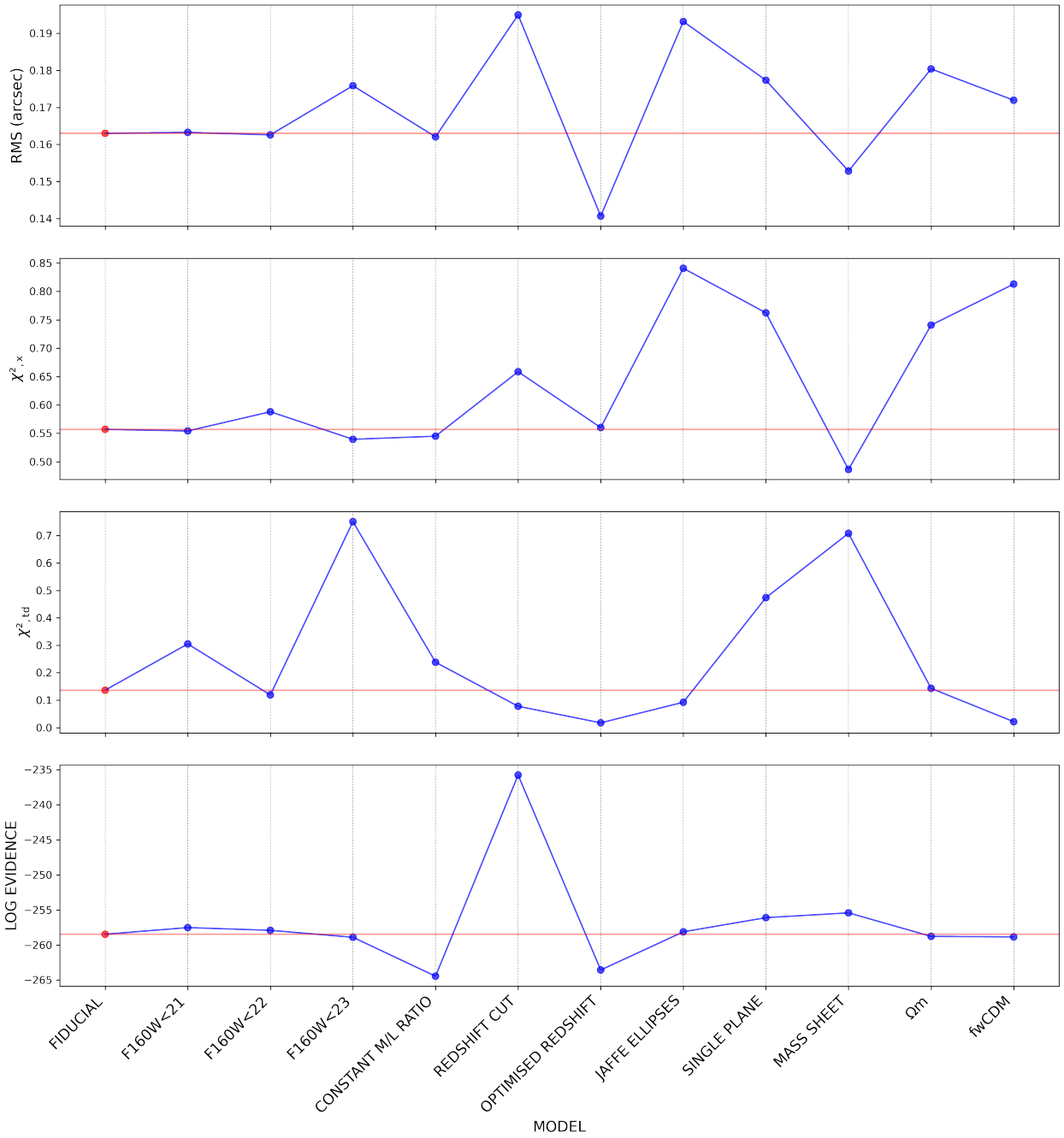

Figure 4.2: Figures of merit for each model. The red dots correspond to the values of the `Fiducial` model while the horizontal line aims to ease the comparisons with the other models. The rms and $\chi^2_{,\mathrm{x}}$ and $\chi^2_{,\mathrm{td}}$ indicate the precision of the model in reproducing the observed multiple images positions and the measured time delay, respectively. Log Evidence combines accuracy and complexity.

There are several differences between statistical indicators for a same model:

- In the `Redshift cut` model, there is a discrepancy between the better quality suggested by the time delay and the worse suggested by positions.
- The same disagreement is present in `Optimised redshift`. Once again, improvements do not always make up for the higher complexity of a model.

- In the `Mass sheet` model time delays are worse predicted than the multiple images positions, but this is further discussed in Subsection 4.2.3.

4.2.2 H_0 inference

Using the MCMC chains obtained from `gravity.jl`, we build the probability density functions for each of the studied models, with their respective statistics.

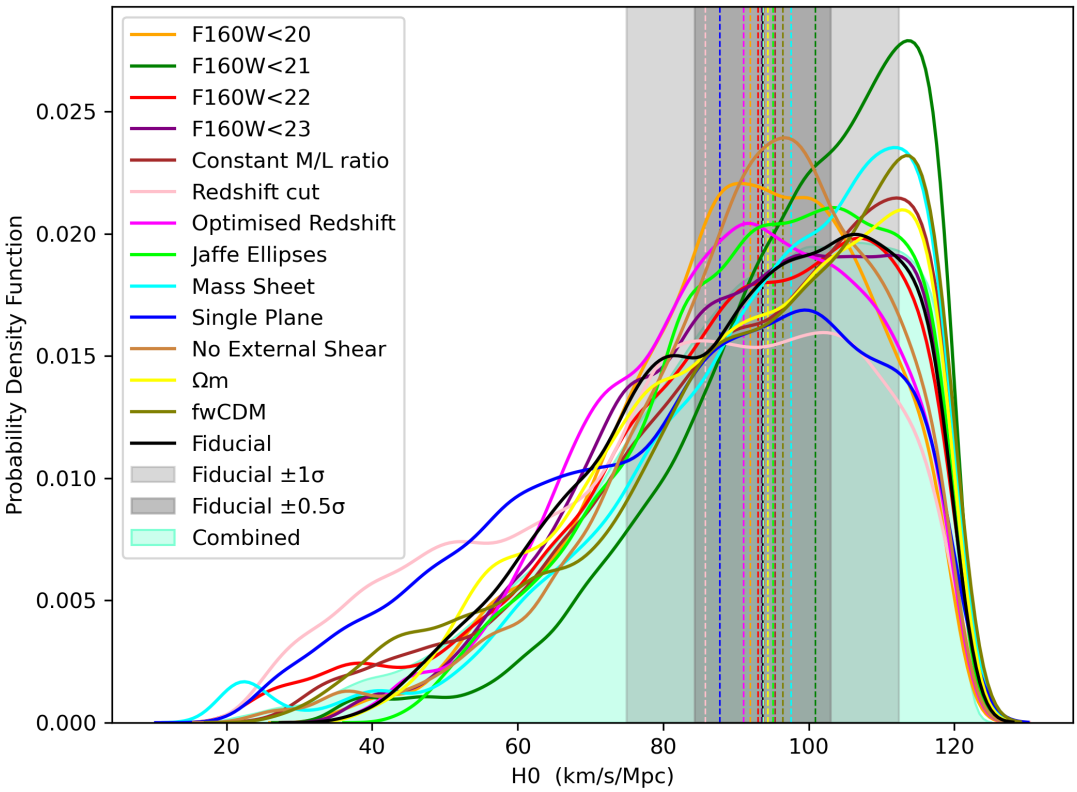

Figure 4.3: Probability density function of H_0 of each of the models explored in this work, summarised in Table 4.1. Vertical, dashed lines represent the median values while the light and dark-shadowed areas are the 0.5σ and 1σ confidence intervals of the `Fiducial` model, respectively. The `Combined` model is created concatenating the chains of all the models.

As can be seen in Figure 4.3, all of the models have consistent distributions, with their median values being not only within the 1σ standard deviation, but also within 0.5σ of the `Fiducial` model. To create the `Combined` model, we have concatenated all the MCMC chains of H_0, shown by the shaded distribution. The sum of all the models shows the inference of the value of H_0, including both the statistical and systematic uncertainties. Both the Hubble constant and the standard deviation are somewhat the same as those of the `Fiducial` model. Therefore, we can conclude that the statistical uncertainty on the H_0 inference with SDSS J1029+2623 is comparable to the systematic one. As a result, we measure a value of $H_0 = 93.7 \pm 20.1$ km s^{-1} Mpc^{-1}, with its 1σ confidence interval.

4.2.3 Mass sheet

In Figure 4.2 we observe that for the `Mass Sheet` model, the time delays are worse predicted than the positions. In fact, the foundation of the mass sheet is maintaining the positions while changing the total mass. Effects on time delay are due to the mass sheet degeneracy, which, even though it can always be present, becomes explicit in this model.

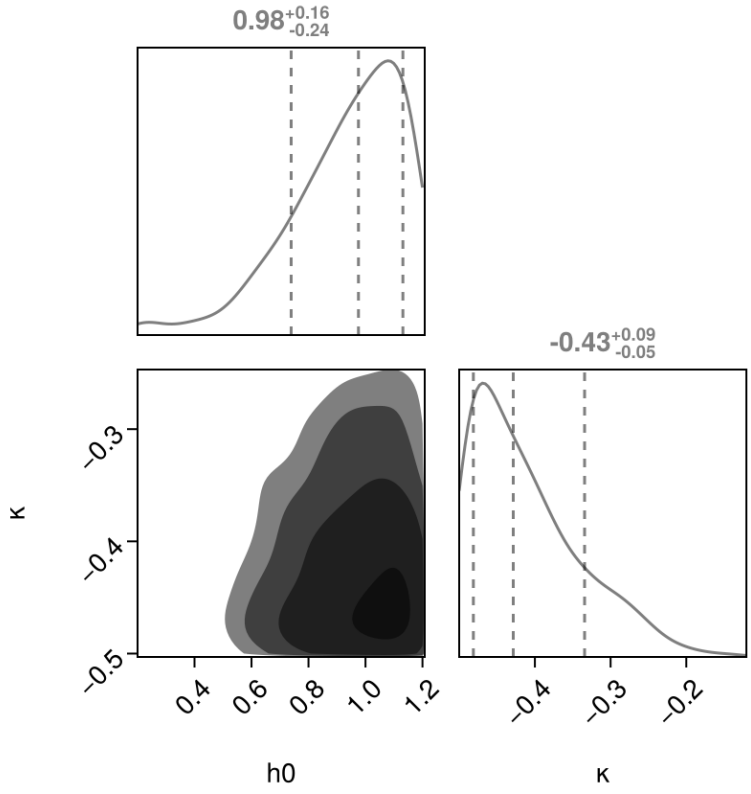

Figure 4.4: Posterior probability distributions of the Hubble constant H_0 and the convergence factor κ from the `Mass sheet` model. Displayed at the top of each column are the median and 1σ values.

We can see in Figure 4.4 how the mass sheet does not introduce a degeneracy for H_0. The inferred value for the mass sheet convergence $\kappa = -0.4 \pm 0.1$, differing from the expected null value. A negative value can either indicate an overestimation of the mass that needs to be compensated or some unexplored systematic uncertainty in the modelling. The latter can also be the reason for the values of H_0, which are larger than those from the CMB Planck (67.3 ± 0.5 km s^{-1} Mpc^{-1}) and the strong lensing value $H_0 = 73 \pm 1.8$ km s^{-1} Mpc^{-1}.

4.2.4 General cosmologies

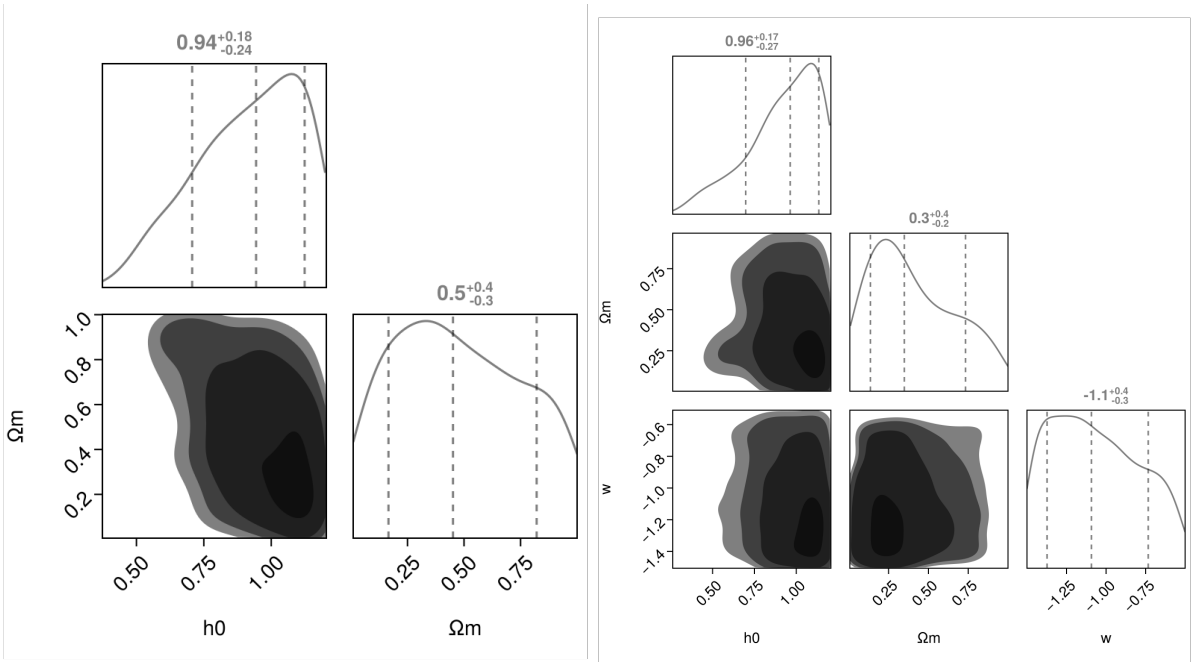

(a) (b)

Figure 4.5: Posterior probability distributions of the Hubble constant H_0, matter density parameter Ω_m (left) and the dark energy equation of state, w (right), obtained from the Ω_m and `fwCDM` models, respectively. Displayed at the top of each column are the median and 1σ values.

In Figure 4.5a, we appreciate a degeneracy between Ω_m and H_0. This can justify the discrepancy with the expected $\Omega_m = 0.3$. For Figure 4.5b, Ω_m shows a degeneracy with H_0. The inferred values from both general cosmologies are compatible with the fΛCDM standard model, given the large statistical uncertainties. Both degeneracies show a anti-correlation between H_0 and Ω_m, which means that for lower values of H_0, we get higher values of Ω_m.

The higher number of degrees of freedom in the models Ω_m and `fwCDM` only enlarges the uncertainties, as summarised in Table 4.2.

Model	**Parameter**	Inferred value	**Relative error** (%)
Ω_m	Ω_m	0.5	70
`fwCDM`	Ω_m	0.3	100
	w	-1.1	30

Table 4.2: Relative errors and inferred values of the cosmological parameters free to vary in Ω_m and `fwCDM` models.

From Table 4.2 we can conclude that strong lensing allows the measurement of w with the highest accuracy (after H_0), followed by Ω_m.

4.3 Testing gravity.jl

4.3.1 Rescaling of the positional uncertainties

We notice, in Table 4.1, that the $\chi^2_{\text{red,x}}$ values are smaller than one. Whenever this happens, it means errors may have been overestimated, because a good statistical uncertainty would have a value of $\chi^2_{\text{red}} \approx 1$.

We have uniformly rescaled the positional errors for all the multiple images by a factor of 0.6. By doing so, one expects that the best-fit and median remain unchanged, where the positional rescaling only affects the broadness of the distribution.

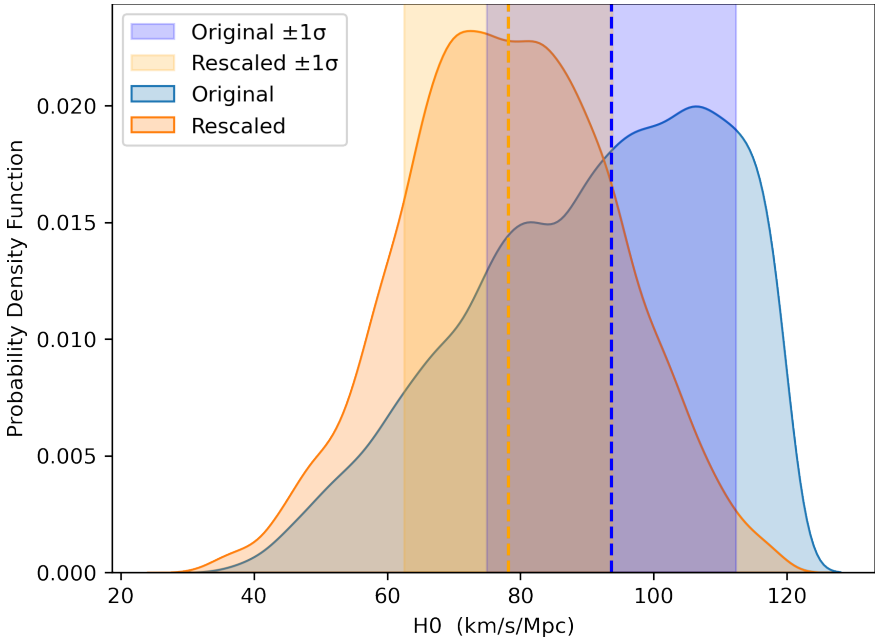

Figure 4.6: Probability density function of `Original fiducial` model and the respective rescaled model with positional errors scaled by a factor of 0.6, implementing variational rounds. Median values and standard deviations are shown as described in the legend.

However, some differences can be observed in Figure 4.6. Both distributions have different median values, although they are consistent within 1σ.

4.3.2 Variational rounds

Initially the `Fiducial` model includes 'variational rounds' in the optimisation scheme. This algorithm option allows for a smarter exchange between the different threads that are being simultaneously run. Variational rounds are meant to improve the results and provide better fits. However, this can turn out to be counterproductive if strong degeneracies are created. We thus explore the impact of the optimisation scheme in the H_0 inference with SDSS J1029+2623.

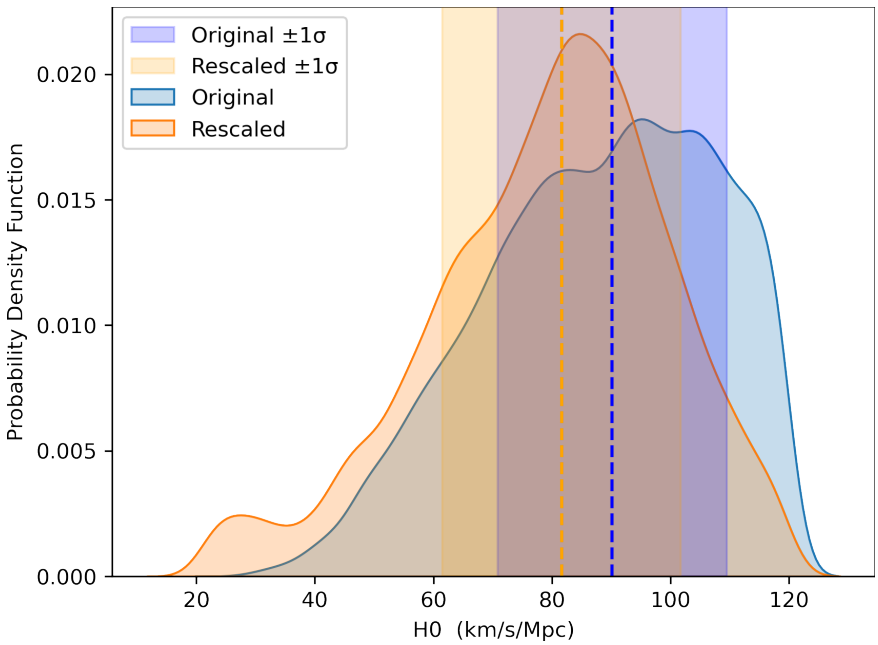

Figure 4.7: Probability density function of models `Original fiducial` model and `Rescaled fiducial` with positional errors scaled by a factor of 0.6, with no variational rounds. Median values and standard deviations are shown as described in the legend.

Figure 4.7 shows a slight improvement with respect to Figure 4.6. Both distributions are in better agreement with each other, in particular their median values. The `Rescaled fiducial` posterior distribution is more peaked, as expected when the positional errors are reduced. This last result can be extended to Figure 4.6. Once again, these results further support the idea that degeneracies probably have the greatest impact on the models.

	Model	$\boldsymbol{H_0}$ (km s^{-1} Mpc^{-1})	**Relative error** (%)
No variational rounds	`Original fiducial`	93.67	19.95
	`Rescaled fiducial`	78.20	20.02
Variational rounds	`Original fiducial`	90.15	21.45
	`Rescaled fiducial`	20.13	24.66

Table 4.3: Values of H_0 and their respective relative error for the all the alternatives of the `Fiducial` model that aim to test the different options for future studies that require `gravity.jl`.

In Table 4.3 we can observe that the relative errors are smaller when not using variational rounds. Therefore, future `gravity.jl` lens models of SDSS J1029+2623 may benefit from not using variational rounds and larger positional uncertainties.

4.4 Discussion

The results obtained in this Chapter suggest SDSS J1029+2623 alone is not a very well-suited system for this cosmological analysis. The main reasons are that the inferred values of H_0 are not compatible with those obtained from other probes, the cosmological parameters are predicted with very high uncertainties, and it infers a mass sheet with a negative convergence.

SDSS J1029+2623 has been more recently modelled in the multiplane formalism in Acebron *et al.* (2024), using the 26 multiple images, as well as the extended surface-brightness distribution of the quasar host galaxy, and light distribution of objects near the quasar host. This is done using the free-form, pixel-grid-based modelling method, where each pixel is individually analysed. A highly accurate inference of the brightness is obtained for the quasar system when compared to the F160W band of HST. This was done aiming to increase the number of observables, that is of the range of tens of thousands for the host galaxy versus the 26 multiple images. A higher number of observables constrains better the total mass distribution of the lensing cluster, and holds the potential of significantly decreasing the uncertainties on the measurement of the value of H_0. In addition to the relatively small number of multiple images, SDSS J1029+2623 has a single measured time delay, which also means fewer constraints on the value of H_0.

The work in Grillo *et al.* (2024) analyses the galaxy cluster MACS J1149.5+2223, which has 89 observed multiple images, substantially more than the 26 found in SDSS J1029+2623. In addition, there are four observed time delays. The cosmological parameters $\Omega_\Lambda = 0.76^{+0.15}_{-0.10}$ (hence $\Omega_m = 0.24$) and $w = -0.92^{+0.15}_{-0.21}$ are measured. H_0 is measured to be $H_0 = 65.1^{+3.5}_{-3.4}$ km s^{-1} Mpc^{-1}, with a relative error $\sim 6\%$, indicating that a larger sample of multiple images and observed time delays provides tighter constraints on the cosmological parameters and considerably improves the precision of this particular parameter.

Other studies, such as those from the TDCOSMO Collaboration *et al.* (2025), use a more extended sample: a combination of lensed systems at galaxy-scale, both with and without time delays, and with resolved and unresolved kinematics. With the data gathered from multiple telescopes, cosmological parameters like H_0 and Ω_m are predicted using and combining different probes. Results from lensing probes for the flat ΛCDM model infer H_0 between $H_0 = 74$ km s^{-1} Mpc^{-1} and $H_0 = 75.1$ km s^{-1} Mpc^{-1}, and relative errors of around $\sim 5.5\%$. However, at the galaxy-scale, the mass-sheet degeneracy becomes relevant and cosmological parameters are more sensitive; hence, other modelling techniques, such as time delays in lensing galaxy clusters, are highly complementary and worth pursuing.

5 Conclusions and perspectives

Conclusions

We have developed and analysed 15 lens models of the SDSS J2019+2623 lens galaxy cluster. Each of the models aimed to study the impact of possible sources of systematic uncertainties, especially on the inferred values of the Hubble constant, H_0 that range between $H_0 = 83.5$ km s^{-1} Mpc^{-1} and $H_0 = 100.9$ km s^{-1} Mpc^{-1}. In these models, we have studied the impact of magnitude truncation of cluster members and different scaling relations to model their mass contribution, removal of high-redshift multiple image systems, optimisation of redshifts; changes in the adopted mass-density profile of the dark matter halos, the inclusion of the external shear, the impact of single- or multi-plane modelling, the presence of a mass sheet, and more general cosmological models than the flat ΛCDM. The `Fiducial` model is the corresponding version of the model analysed in Acebron *et al.* (2022b) with the new lensing modelling software `gravity.jl`, for which we obtained an inferred value of $H_0 = 93.7 \pm 18.7$ km s^{-1} Mpc^{-1}. We have found that all of the models estimated H_0 values are in agreement with the `Fiducial` one within 1σ of the `Fiducial` model. This indicates that the studied systematic uncertainties are not as relevant as we could expect given that, for this particular lens system, statistical errors dominate the total error budget. We can also see how the H_0 value obtained for the `Fiducial` model is far from solving the Hubble tension, that contemplates values of the Hubble constant between $H_0 = 67.3 \pm 0.5$ km s^{-1} Mpc^{-1} and $H_0 = 73.0 \pm 1.8$ km s^{-1} Mpc^{-1}.

We have used four different statistical estimators to assess the goodness of the models: rms, $\chi^2_{\rm red,x}$, $\chi^2_{\rm ,td}$ and Log Evidence. The impact of the systematics varies depending on the indicator we use. Combining all the models and, hence, accounting for all the systematics, the distribution for the `Combined` model is very similar to the `Fiducial` model, with a median of $H_0 = 93.7 \pm 20.1$ km s^{-1} Mpc^{-1}. This indicates that the `Fiducial` model is a good approximation for all the uncertainty sources we have studied. Even though some of the estimators suggest there are better models than the `Fiducial` model, this is just from a statistical point of view. Statistical and systematic errors are in fact comparable.

The lack of a degeneracy between the values of H_0 and κ in the `Mass sheet` model is a common feature of cluster-scale lensing. However, for this system, we observe a negative convergence factor of $\kappa = -0.4 \pm 0.1$. This value suggests the mass-density profile has been overestimated at some point along the line of sight. Another explanation could be a misinterpretation of the model, that would explain the unexpectedly high values of H_0.

Regarding the cosmological models considered in this work we conclude that our measurements of Ω_m and w from strong gravitational lensing alone and this particular system provide values that are consistent with the flat ΛCDM model. In both the Ω_m and `fwCDM` models we see a slight

negative degeneracy between Ω_m and H_0, as well as very large statistical uncertainties. For the Ω_m model we obtain $\Omega_m = 0.5^{+0.4}_{-0.3}$. For the `fwCDM` model we obtain $\Omega_m = 0.3^{+0.4}_{-0.2}$ and $w = -1.1^{+0.4}_{-0.3}$. We have thus found that H_0 is the most precisely measured cosmological parameter, with a relative error around 20%. It is followed by w, and finally Ω_m, with relative errors of 30% and up to 100%, respectively.

Finally, regarding the software `gravity.jl` we can say that no major differences are found from the use of variational rounds or underestimated positional errors. However, in both cases, we observe a tendency towards lower values of H_0 and more peaked distributions.

Perspectives

Strong lensing is a promising tool to probe the expansion rate and geometry of the Universe through time delay cosmography and eventually solve the Hubble tension. There are two paths that will lead to great progress: statistical and technical advances.

Currently, there are few cluster-lensed quasar with high-precision measured time delays. A larger sample of such extraordinary systems would lead to a reduction in statistical and systematic uncertainties and more stringent measurements of the values of the cosmological parameters. In addition to that, this analysis could also benefit from a larger sample of observables that could either come from a larger number of multiple images or the direct inclusion of the surface-brightness of the strongly-lensed observables from the host galaxy. In addition, increasing the number of time delay observations can turn out to be very helpful. For example, SDSS J2222+2745, studied in Acebron *et al.* (2022a), only has 12 multiple images from 3 background sources. What makes this system interesting is that 6 out of the 12 multiple images belong to the quasar and two time delays are measured. Relevant advances are expected from SDSS J2222+2745 with the upcoming instrumental improvements (JWST, Vera Rubin, Euclid).

Regarding the technical aspects, we are now entering the golden era of strong lensing thanks to the advent of wide-field surveys field. On Earth, we will soon have the Vera Rubin Observatory, located in Chile. Vera Rubin will have the best digital camera so far built to observe the southern sky during 10 years with the Legacy Survey of Space and Time (LSST), that will study transient in the Universe. The Vera Rubin Observatory is expected to find thousands of lens systems and several dozens of cluster-lensed quasars. This can be particularly useful to measure their time delays and determine the Hubble constant.

Another instrument that will support the development of strong lensing is the Euclid mission. Euclid is focused on studying dark matter, dark energy, and the geometry by observing one third of the sky.

The JWST has already been exploring the Universe for a few years and will allow to improve the individual lens models of these rare galaxy clusters. It is located on the Lagrange point L2, where gravitational forces of the Sun and the Earth are in equilibrium. In L2, we have thermal stability and a clear vision of the sky. We are expecting open access near-infrared observations of SDSS J1029+2623 in the upcoming months. The JWST spans a wavelength range focused on the red and infrared spectrum, which will help us find high-redshift multiple image systems that become visible in the infrared.

In the foreseeable future, the deep, infrared data we will obtain from the JWST, together with the wide-field surveys with Euclid and the Vera Rubin Observatory, that will find thousands of new lens systems; will strengthen gravitational lensing and help us solve the Hubble tension. Hopefully, we will then be able to understand the physics that govern the Universe.

Bibliography

1. Refsdal, S. On the possibility of determining Hubble's parameter and the masses of galaxies from the gravitational lens effect. *Monthly Notices of the Royal Astronomical Society* **128,** 307. doi:10.1093/mnras/128.4.307 (Jan. 1964).
2. Kormann, R., Schneider, P. & Bartelmann, M. Isothermal elliptical gravitational lens models. *Astronomy and Astrophysics* **284,** 285–299 (Apr. 1994).
3. Keeton, C. R. A Catalog of Mass Models for Gravitational Lensing. *arXiv e-prints,* astro–ph/0102341. doi:10.48550/arXiv.astro-ph/0102341. arXiv: astro-ph/0102341 [astro-ph] (Feb. 2001).
4. Knudson, A., Ratnatunga, K. U. & Griffiths, R. E. Investigation of Gravitational Lens Mass Models. *The Astronomical Journal* **122,** 103–112. doi:10.1086/321122. arXiv: astro-ph/0104123 [astro-ph] (July 2001).
5. Claeskens, J. .-., Sluse, D., Riaud, P. & Surdej, J. Multi wavelength study of the gravitational lens system RXS J1131-1231. II. Lens model and source reconstruction. *Astronomy and Astrophysics* **451,** 865–879. doi:10.1051/0004-6361:20054352. arXiv: astro-ph/0602309 [astro-ph] (June 2006).
6. Clowe, D. *et al.* A Direct Empirical Proof of the Existence of Dark Matter. *The Astrophysical Journal Letters* **648,** L109–L113. doi:10.1086/508162. arXiv: astro-ph/0608407 [astro-ph] (Sept. 2006).
7. Inada, N. *et al.* SDSS J1029+2623: A Gravitationally Lensed Quasar with an Image Separation of 22.5". *The Astrophysical Journal Letters* **653,** L97–L100. doi:10.1086/510671. arXiv: astro-ph/0611275 [astro-ph] (Dec. 2006).
8. Schneider, P., Kochanek, C. S. & Wambsganss, J. *Gravitational Lensing: Strong, Weak and Micro* (eds Meylan, G. *et al.*) doi:10.48550/arXiv.astro-ph/0407232. arXiv: astro-ph/0407232 [astro-ph] (Jan. 2006).
9. Jullo, E. *et al.* A Bayesian approach to strong lensing modelling of galaxy clusters. *New Journal of Physics* **9,** 447. doi:10.1088/1367-2630/9/12/447. arXiv: 0706.0048 [astro-ph] (Dec. 2007).
10. Oguri, M. *et al.* The Third Image of the Large-Separation Lensed Quasar SDSS J1029+2623. *The Astrophysical Journal Letters* **676,** L1. doi:10.1086/586897. arXiv: 0802.0002 [astro-ph] (Mar. 2008).
11. Ota, N. *et al.* The Chandra View of the Largest Quasar Lens SDSS J1029+2623. *The Astrophysical Journal* **758,** 26. doi:10.1088/0004-637X/758/1/26. arXiv: 1202.1645 [astro-ph.CO] (Oct. 2012).
12. Fohlmeister, J. *et al.* A Two-year Time Delay for the Lensed Quasar SDSS J1029+2623. *The Astrophysical Journal* **764,** 186. doi:10.1088/0004-637X/764/2/186. arXiv: 1207.5776 [astro-ph.CO] (Feb. 2013).
13. Oguri, M. *et al.* The Hidden Fortress: structure and substructure of the complex strong lensing cluster SDSS J1029+2623. *Monthly Notices of the Royal Astronomical Society* **429,** 482–493. doi:10.1093/mnras/sts351. arXiv: 1209.0458 [astro-ph.CO] (Feb. 2013).
14. Oguri, M. *et al.* The Hidden Fortress: structure and substructure of the complex strong lensing cluster SDSS J1029+2623. *Monthly Notices of the Royal Astronomical Society* **429,** 482–493. doi:10.1093/mnras/sts351. arXiv: 1209.0458 [astro-ph.CO] (Feb. 2013).
15. Schneider, P. & Sluse, D. Mass-sheet degeneracy, power-law models and external convergence: Impact on the determination of the Hubble constant from gravitational lensing. *Astronomy and Astrophysics* **559,** A37. doi:10.1051/0004-6361/201321882. arXiv: 1306.0901 [astro-ph.CO] (Nov. 2013).
16. Planck Collaboration *et al.* Planck 2013 results. XVI. Cosmological parameters. *Astronomy and Astrophysics* **571,** A16. doi:10.1051/0004-6361/201321591. arXiv: 1303.5076 [astro-ph.CO] (Nov. 2014).
17. Jackson, N. The Hubble Constant. *Living Reviews in Relativity* **18,** 2. doi:10.1007/lrr-2015-2 (Dec. 2015).
18. Schneider, P. *Extragalactic Astronomy and Cosmology: An Introduction* doi:10.1007/978-3-642-54083-7 (Springer-Verlag, 2015).

19. Grillo, C. *et al.* Measuring the Value of the Hubble Constant "à la Refsdal". *The Astrophysical Journal* **860,** 94. doi:10.3847/1538-4357/aac2c9. arXiv: 1802.01584 [astro-ph.CO] (June 2018).
20. Bergamini, P. *et al.* Enhanced cluster lensing models with measured galaxy kinematics. *Astronomy and Astrophysics* **631,** A130. doi:10.1051/0004-6361/201935974. arXiv: 1905.13236 [astro-ph.GA] (Nov. 2019).
21. Grillo, C. *et al.* On the Accuracy of Time-delay Cosmography in the Frontier Fields Cluster MACS J1149.5+2223 with Supernova Refsdal. *The Astrophysical Journal* **898,** 87. doi:10.3847/1538-4357/ab9a4c. arXiv: 2001.02232 [astro-ph.CO] (July 2020).
22. Wong, K. C. *et al.* H0LiCOW - XIII. A 2.4 per cent measurement of H_0 from lensed quasars: 5.3σ tension between early- and late-Universe probes. *Monthly Notices of the Royal Astronomical Society* **498,** 1420–1439. doi:10.1093/mnras/stz3094. arXiv: 1907.04869 [astro-ph.CO] (Oct. 2020).
23. Acebron, A. *et al.* New strong lensing modelling of SDSS J2222+2745 enhanced with VLT/MUSE spectroscopy. *Astronomy and Astrophysics* **668,** A142. doi:10.1051/0004-6361/202244836. arXiv: 2208.13788 [astro-ph.GA] (Dec. 2022).
24. Acebron, A. *et al.* VLT/MUSE Observations of SDSS J1029+2623: Toward a High-precision Strong Lensing Model. *The Astrophysical Journal* **926,** 86. doi:10.3847/1538-4357/ac3d35. arXiv: 2111.05871 [astro-ph.GA] (Feb. 2022).
25. Caminha, G. B., Suyu, S. H., Grillo, C. & Rosati, P. Galaxy cluster strong lensing cosmography. Cosmological constraints from a sample of regular galaxy clusters. *Astronomy and Astrophysics* **657,** A83. doi:10.1051/0004-6361/202141994. arXiv: 2110.06232 [astro-ph.CO] (Jan. 2022).
26. Riess, A. G. *et al.* A Comprehensive Measurement of the Local Value of the Hubble Constant with 1 km s^{-1} Mpc^{-1} Uncertainty from the Hubble Space Telescope and the SH0ES Team. *The Astrophysical Journal Letters* **934,** L7. doi:10.3847/2041-8213/ac5c5b. arXiv: 2112.04510 [astro-ph.CO] (July 2022).
27. Bergamini, P. *et al.* A state-of-the-art strong-lensing model of MACS J0416.1−2403 with the largest sample of spectroscopic multiple images. *Astronomy and Astrophysics* **674,** A79. doi:10.1051/0004-6361/202244834. arXiv: 2208.14020 [astro-ph.CO] (June 2023).
28. European Space Agency. *Euclid overview* Last updated 24 January 2023. ESA. https://www.esa.int/Science_Exploration/Space_Science/Euclid/Euclid_overview (2025).
29. Napier, K. *et al.* Hubble Constant Measurement from Three Large-separation Quasars Strongly Lensed by Galaxy Clusters. *The Astrophysical Journal* **959,** 134. doi:10.3847/1538-4357/ad045a. arXiv: 2301.11240 [astro-ph.CO] (Dec. 2023).
30. Acebron, A. *et al.* The Next Step in Galaxy Cluster Strong Lensing: Modeling the Surface Brightness of Multiply Imaged Sources. *The Astrophysical Journal* **976,** 110. doi:10.3847/1538-4357/ad8343. arXiv: 2410.01883 [astro-ph.GA] (Nov. 2024).
31. Di Valentino, E. & Brout Dillon. *The Hubble Constant Tension* doi:10.1007/978-981-99-0177-7 (2024).
32. ESA Webb. *Gravitational Lensing* Accessed: 18 Mar. 2025. 2024. https://esawebb.org/wordbank/gravitational-lensing/.
33. Grillo, C., Pagano, L., Rosati, P. & Suyu, S. H. Cosmography with supernova Refsdal through time-delay cluster lensing: Independent measurements of the Hubble constant and geometry of the Universe. *Astronomy and Astrophysics* **684,** L23. doi:10.1051/0004-6361/202449278. arXiv: 2401.10980 [astro-ph.CO] (Apr. 2024).
34. Harvard-Smithsonian Center for Astrophysics. *Gravitational Lensing* Accessed: 18 Mar. 2025. 2024. https://www.cfa.harvard.edu/research/topic/gravitational-lensing.
35. Lombardi, M. Gravity.jl: Fast and accurate gravitational lens modeling in Julia: I. Point-like and linearized extended sources. *Astronomy and Astrophysics* **690,** A346. doi:10.1051/0004-6361/202451214. arXiv: 2406.15280 [astro-ph.IM] (Oct. 2024).
36. Natarajan, P. *et al.* Strong Lensing by Galaxy Clusters. *Space Science Reviews* **220,** 19. doi:10.1007/s11214-024-01051-8. arXiv: 2403.06245 [astro-ph.CO] (Feb. 2024).
37. Buncher, B., Holder, G. & Hotinli, S. Gravitational Lensing of Galaxy Clustering. *The Open Journal of Astrophysics* **8,** 30. doi:10.33232/001c.132332. arXiv: 2402.07988 [astro-ph.CO] (Mar. 2025).
38. TDCOSMO Collaboration *et al.* TDCOSMO 2025: Cosmological constraints from strong lensing time delays. *arXiv e-prints,* arXiv:2506.03023. doi:10.48550/arXiv.2506.03023. arXiv: 2506.03023 [astro-ph.CO] (June 2025).

39. IBM Corporation. *Monte Carlo simulation* https://www.ibm.com/think/topics/monte-carlo-simulation (2025).

40. NASA. *Hubble Space Telescope – Overview* National Aeronautics and Space Administration. https://science.nasa.gov/mission/hubble/overview/about-hubble/ (2025).

41. NASA. *James Webb Space Telescope – Overview* National Aeronautics and Space Administration. https://science.nasa.gov/mission/webb/about-overview/ (2025).

42. Vera C. Rubin Observatory / LSST Corporation. *Science goals of the Vera C. Rubin Observatory* Vera C. Rubin Observatory. https://rubinobservatory.org/explore/science-goals (2025).